Molecular Biology and Evolution, 2025, **42**, 1–24
https://doi.org/10.1093/molbev/msaf017
Advance access publication 21 January 2025
Discoveries

MBE OXFORD

Single-cell and Spatial Transcriptomics Illuminate Bat Immunity and Barrier Tissue Evolution

Roy Levinger [1,†] Dafna Tussia-Cohen [1,†] Sivan Friedman [1] Yan Lender,[1] Yomiran Nissan [2] Evgeny Fraimovitch [1] Yuval Gavriel [1] Jacqueline L. E. Tearle [3,4] Aleksandra A. Kolodziejczyk [5] Kyung-Mee Moon [6,7] Tomás Gomes [8] Natalia Kunowska,[9] Maya Weinberg [2] Giacomo Donati [10,11] Leonard J. Foster [6,7] Kylie R. James [3,4] Yossi Yovel [2,12] Tzachi Hagai [1,*]

[1]Shmunis School of Biomedicine and Cancer Research, George S Wise Faculty of Life Sciences, Tel Aviv University, Tel Aviv 69978, Israel
[2]School of Zoology, George S. Wise Faculty of Life Sciences, Tel Aviv University, Tel Aviv 69978, Israel
[3]Translational Genomics, Garvan Institute of Medical Research, Sydney, New South Wales, Australia
[4]School of Biomedical Sciences, University of New South Wales, Sydney, Australia
[5]International Institute of Molecular and Cellular Biology, Warsaw, Poland
[6]Michael Smith Laboratories, University of British Columbia, Vancouver, BC, Canada
[7]Biochemistry and Molecular Biology Department, University of British Columbia, Vancouver, BC, Canada
[8]Fundação GIMM - Gulbenkian Institute for Molecular Medicine, Avenida Professor Egas Moniz, 1649-028 Lisboa, Portugal
[9]Institute of Pharmaceutical Sciences, University of Graz, Graz, Austria
[10]Department of Life Sciences and Systems Biology, University of Turin, Torino, Italy
[11]Molecular Biotechnology Center, University of Turin, Torino, Italy
[12]Sagol School of Neuroscience, Tel Aviv University, Tel Aviv 6997801, Israel

[†]These authors contributed equally.
***Corresponding author:** E-mail: tzachiha@tauex.tau.ac.il.
Associate editor: Katja Nowick

Abstract

Bats have adapted to pathogens through diverse mechanisms, including increased resistance—rapid pathogen elimination, and tolerance—limiting tissue damage following infection. In the Egyptian fruit bat (an important model in comparative immunology), several mechanisms conferring disease tolerance were discovered, but mechanisms underpinning resistance remain poorly understood. Previous studies on other species suggested that the elevated basal expression of innate immune genes may lead to increased resistance to infection. Here, we test whether such transcriptional patterns occur in Egyptian fruit bat tissues through single-cell and spatial transcriptomics of gut, lung, and blood cells, comparing gene expression between bat, mouse, and human. Despite numerous recent loss and expansion events of interferons in the bat genome, interferon expression and induction are remarkably similar to that of mouse. In contrast, central complement system genes are highly and uniquely expressed in key regions in bat lung and gut epithelium, unlike in human and mouse. Interestingly, the unique expression of these genes in the bat gut is strongest in the crypt, where developmental expression programs are highly conserved. The complement system genes also evolve rapidly in their coding sequences across the bat lineage. Finally, the bat complement system displays strong hemolytic activity. Together, these results indicate a distinctive transcriptional divergence of the complement system, which may be linked to bat resistance, and highlight the intricate evolutionary landscape of bat immunity.

Keywords: bats, comparative transcriptomics, evolution of immune defenses, tissue evolution, single-cell transcriptomics

Introduction

Accounting for ~20% of all mammals and distributed across the globe, bats constitute a large and ecologically diverse clade that evolved several unique adaptations, including powered flight, echolocation, and extreme longevity. Several bat species display mild or no clinical symptoms when infected by some of the viruses deadliest to humans (Li et al. 2005; Field et al. 2007; Ge et al. 2013; Amman et al. 2017), they are suspected to be the natural reservoir for several of these viruses and the potential source of recent zoonotic transfers to humans (Li et al. 2005; Banerjee et al. 2019; Zhou et al. 2020; Temmam et al. 2022). The mechanisms of bat adaptation to these viruses and to other pathogens have been a continuous source of interest, leading to numerous studies that focused on the immune systems of different bat species (Irving et al. 2021). These studies found evolutionary changes in specific genes, such as in recent duplication and rapid coding sequence evolution of antiviral restriction factors (Hayward et al. 2022; Jacquet et al. 2022; Schneor et al. 2023), and in entire pathways, such as in dampening the inflammasome-mediated response through diverse mechanisms (Irving et al. 2021; Ahn et al. 2023). To detect these potentially adaptive evolutionary changes, specific immune genes and pathways are often compared between bats and the corresponding genes and

Received: September 29, 2024. **Revised:** November 26, 2024. **Accepted:** January 14, 2025

pathways in mouse and human that have well-characterized immune systems with different historical exposures to pathogens (Kuzmin et al. 2017; Moreno Santillán et al. 2021; Hayward et al. 2022; Jacquet et al. 2022; Jayaprakash et al. 2023; Schneor et al. 2023; Tian et al. 2023; Cagliani et al. 2024). Interestingly, it was suggested that while some bat species have evolved mechanisms of increased "disease resistance", the ability to rapidly and efficiently inhibit infection, other bats have adapted through increased "disease tolerance", containment of infection while avoiding an excessive immune reaction (Schountz et al. 2017; Banerjee et al. 2020; Vicente-Santos et al. 2023; Demian et al. 2024).

The Egyptian fruit bat (*Rousettus aegyptiacus*) is a megabat thought to serve as the natural reservoir of the highly pathogenic Marburgvirus (a filovirus related to Ebolavirus) (Amman et al. 2017). In addition, *R. aegyptiacus* infection with Ebolavirus is asymptomatic, despite successful viral replication in bat tissues (Paweska et al. 2016; Guito et al. 2021; Jayaprakash et al. 2023). As such, *R. aegyptiacus* is considered an important model for studying the mechanisms of immune adaptation to infection, and was proposed as one of the key bat species for comprehensive immune characterization (Wang et al. 2021). Previous studies of the immune system of *R. aegyptiacus* have so far discovered various molecular mechanisms that can promote disease tolerance. These include genomic findings of the expansion of gene families related to inhibitory immune states (Pavlovich et al. 2018) and the loss of short pentraxins (Larson et al. 2021) that are involved in acute phase response in humans. Additionally, a transcriptomics analysis that compared the in vitro antiviral response between bat species, pointed to species-specific strong upregulation of genes associated with disease tolerance in *R. aegyptiacus* cells (Schneor et al. 2023). Finally, analyses of *R. aegyptiacus* response to in vivo filovirus infection revealed reduced proinflammatory gene induction in response to infection (Guito et al. 2021; Jayaprakash et al. 2023). These findings bolster the notion that increased tolerance to infection in the form of a limited inflammatory response, assists in reduced tissue damage and serves as an adaptive mechanism in *R. aegyptiacus*. In contrast to this, mechanisms associated with increased resistance have so far remained largely unexplored in *R. aegyptiacus*.

Increased resistance to infection can be achieved by several mechanisms, including elevated levels of innate immune genes in basal conditions, before the infecting pathogen invaded the cells. Elevated levels of innate immune genes, some of which act as viral sensors and some as restriction factors, can result in faster and more effective response against pathogens. Such elevated levels of expression in steady-state conditions were observed in cells of several rodents and in bat species and were suggested to assist in pathogen removal (Zhou et al. 2016; Irving et al. 2020; Cohn et al. 2022). Novel genomics techniques, including single-cell and spatial transcriptomics, can be harnessed to detect differences in orthologous gene expression between species, by comparing these orthologs' levels in homologous cells and in specific tissue regions in high resolution. Such comparisons can identify innate immune genes that are highly expressed in *R. aegyptiacus* cells in comparison with their levels in homologous cells in different mammals. To this end, we created a comprehensive atlas of *R. aegyptiacus* single-cell transcriptomes from lung and gut tissues, two barrier tissues that are central sites for infection through different infection routes and of different pathogens related to bats, and also profiled peripheral blood mononuclear cells (PBMCs) (Fig. 1a). We further profiled an equivalent set of mouse cells in a comparative manner and used publicly available single-cell data from human tissues to find transcriptionally conserved and divergent genes and pathways in *R. aegyptiacus* tissues. We combined this with spatial transcriptomics, innate immune triggering of PBMCs, serum proteomics and functional assays. Taking a comparative genomics approach, we searched for significant transcriptional changes between homologous cells in the three species. The levels of innate immune genes in barrier tissues in unstimulated conditions may represent the "readiness level" in these tissues for pathogens that can infect them. We focused on two important innate pathways: (1) Type-I interferons (IFNs)—a family of cytokines usually expressed following infection, whose main function is to shift cells into an antiviral state. (2) The complement system—a system composed of a cascade of proteins with several innate immune functions, including phagocytosis, cell membrane rupturing and promotion of inflammation. Our findings provide comparative and quantitative insights into regulatory constraints and transcriptional evolution of the bat immune system.

Results

An Integrated Transcriptional Map of *Rousettus aegyptiacus* Blood, Lung and Intestinal Cells

To investigate transcriptional patterns in *R. aegyptiacus* tissues in high resolution, we performed comprehensive single-cell RNA sequencing (scRNA-seq) of Peripheral Blood Mononuclear cells (PBMC) and of cells from the upper gut section and lung of 5 to 8 bat individuals (Fig. 1a). For comparison, we also performed identical processing and profiling procedures on mouse lung and PBMC samples, and on mouse Small Intestine (SI) and colon samples. With both *R. aegyptiacus* and mouse tissues, we employed similar tissue dissociation procedures to those used with previously published human sample datasets (Elmentaite et al. 2021; Madissoon et al. 2023), to minimize technical differences between samples from the three species. Single-cell data were mapped to genomes, followed by dimensionality reduction, clustering, and cell lineages annotations (see "Materials and Methods").

In each tissue, we annotated *R. aegyptiacus* cell clusters and compared them to homologous cell populations in human and mouse. This was achieved by employing EggNOG (Huerta-Cepas et al. 2019) to identify orthology relationship in a genome-wide manner between *R. aegyptiacus*, mouse and human coding genes, followed by manual inspection and further annotations (supplementary table S1, Supplementary Material online). We then used computationally derived and experimentally established markers of various cell types, to associate *R. aegyptiacus* cell clusters with their likely cell lineages. These cell identifications were confirmed by whole-transcriptome correlation analyses of cell clusters between the three species.

We profiled 59,443 bat PBMCs in steady-state conditions as well as following immune stimulation (see details below). Among the profiled PBMCs, we identified 20 major cell populations with homologous cell clusters in mouse and human (Fig. 1b and supplementary figs. S1 to S4, Supplementary Material online). In the lung, we profiled 60,000 high-quality bat cells and identified 45 cell clusters (Fig. 1c and supplementary figs. S5 to S8, Supplementary Material online). In the gut, the data included 46,316 cells in 38 intestinal cell

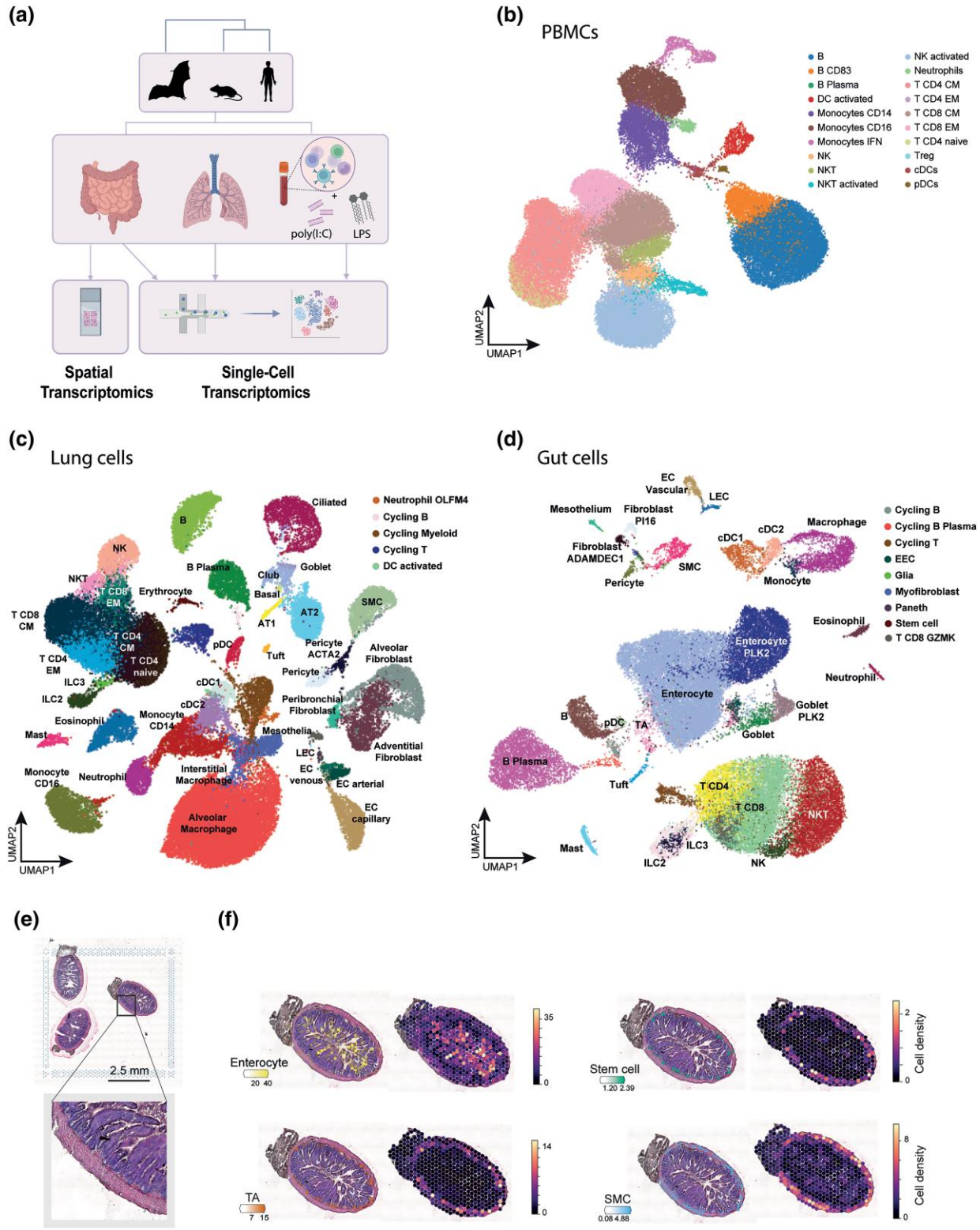

Fig. 1. Characterization of *R. aegyptiacus* cells. a) System overview: Gut- and lung-resident cells from *R. aegyptiacus* and mouse were profiled using single-cell transcriptomics. PBMCs were profiled in steady-state and following the triggering of the antiviral and antibacterial innate immune responses using dsRNA (poly I:C) and LPS, respectively. *R. aegyptiacus* gut samples were also characterized using spatial transcriptomics analysis. *R. aegyptiacus* and mouse cells from this study along with publicly available human cells in each of the respective tissues were compared using one-to-one orthologous genes and following gene orthology assignments using EggNOG. The figure was created in BioRender (2025) https://BioRender.com/b35s117. b) UMAP of *R. aegyptiacus* PBMC clusters (five samples, $n = 59{,}443$ cells). UMAP of mouse PBMCs and cross-species comparisons appear in supplementary figs. S1 to S4, Supplementary Material online. c) UMAP of *R. aegyptiacus* lung cell clusters (10 samples, $n = 60{,}000$ cells). UMAP of mouse lung cells and cross-species comparisons appear in supplementary figs. S5 to S8, Supplementary Material online. d) UMAP of *R. aegyptiacus* intestinal cell clusters (8 samples, $n = 46{,}316$ cells). UMAP of mouse cells and cross-species comparisons appear in supplementary data figs. S9 to S13, Supplementary Material online. e) Hematoxylin and eosin (H&E) staining of transverse cross-section of *R. aegyptiacus* gut ($n = 3$ samples). f) Spatial mapping of scRNA-Seq data to 10× Genomics Visium spatial transcriptomics data, showing estimated abundance (color intensity) of cell subsets (color) of a cross-section using Cell2location.

subsets (Fig. 1d and supplementary figs. S9 to S13, Supplementary Material online). In addition, in the *R. aegyptiacus* gut we inferred cell localization by performing spatial transcriptomics of gut sections, required for several analyses described below (Fig. 1e, f and supplementary fig. S14, Supplementary Material online).

R. aegyptiacus gut morphology has not been comprehensively characterized at the molecular and cellular levels. As in other megabats (Tedman and Hall 1985), and unlike in human and mouse, there are no clear macro-morphological differences between various gut regions (Selim and El Nahas 2015). We thus collected bat gut samples from regions analogous of the jejunum-ileum in the SI. We further verified that these samples have similar morphology to SI morphology (Fig. 1e) and that the bat enterocytes have similar expression to enterocytes from SI of mouse and human (supplementary fig. S15, Supplementary Material online and "Materials and Methods")

Basal Expression of IFN Genes and Their Regulators in *Rousettus aegyptiacus* Cells

We begin our focused analysis of innate immune genes in *R. aegyptiacus*, with the IFN pathway, given its central role in the innate immune response. Previous studies on a different megabat species, *Pteropus alecto*, found elevated levels of IFN genes and the IFN regulators IRF1,3, and 7, in steady-state conditions (i.e. in uninfected and unstimulated cells) (Zhou et al. 2014, 2016; Irving et al. 2020). This increased expression was suggested to assist in rapid inhibition of pathogens (Zhou et al. 2014, 2016; Irving et al. 2020). We investigated whether such patterns occur in *R. aegyptiacus* cells. First, we tested whether Interferon Regulatory Factors (IRF) genes are more highly expressed in bat cells in comparison with human and mouse cells. We performed differential expression (DE) analysis between homologous cell clusters between bat, mouse, and human to find transcriptionally divergent genes (supplementary tables S2 to S5, Supplementary Material online). We observed that IRF genes do not display significant differences between bat, human, and mouse in the tested cells in a strong and consistent manner (supplementary table S6, Supplementary Material online): There are only a few cell types where IRF3 or 7 have expression levels higher than those in human or mouse cells (IRF1 is not annotated in *R. aegyptiacus* genome). These cases of higher expression in bats are not consistent in the terms of comparison to both human and mouse orthologs and when considering both IRF paralogs.

Next, we observed that *R. aegyptiacus* cells are similar to human and mouse homologous cells and do not display significant expression levels of type-I IFNs in steady-state conditions. This was the case in all tissues we profiled and is in agreement with data from previous bulk RNA studies of *R. aegyptiacus* different cell lines and primary tissues where the bats and cells were not infected or immune-stimulated (Jayaprakash et al. 2023; Schneor et al. 2023). In summary, these findings suggest conserved expression patterns of IFN and their IRF regulators across *R. aegyptiacus*, human and mouse cells in steady-state conditions.

Monocytes are the Most Transcriptionally Responsive Cells in Initial Stages of the Innate Immune Response in Both *Rousettus aegyptiacus* and Mouse

Following the observed similarity in the expression of IFN-related genes in basal conditions between mouse and bat, we next asked whether IFN genes transcriptionally diverge in induction, following immune stimulation. In particular, multiple events of loss and expansion of various type-I IFN genes were observed in *R. aegyptiacus* genome (Pavlovich et al. 2018). We thus asked whether the transcriptional induction of IFN genes in *R. aegyptiacus* differs (i) between various *R. aegyptiacus* IFN paralogs, and (ii) between *R. aegyptiacus* IFN genes with respect to IFNs in mouse. To study the induction of IFN in a comparative manner across cells, we stimulated *R. aegyptiacus* and mouse PBMCs with two pathogen-associated molecular patterns (PAMPs): dsRNA (poly I:C) and lipopolysaccharide (LPS), which respectively trigger the antiviral and the antibacterial responses (Fig. 2a). Using the stimulated PBMC data, below we first compare the overall innate immune response between cell types and between the two species. In the sections that follow, we then focus on IFN expression.

When comparing the transcriptional response between cell clusters, we observed that in both antiviral and antibacterial responses and in both mouse and *R. aegyptiacus*, monocytes have the highest numbers of DE genes (supplementary table S7, Supplementary Material online). We next used three previously described sets of innate immune genes, to study which cell clusters tend to upregulate them and how conserved this expression profile is between mouse and *R. aegyptiacus* cells (Fig. 2b and c). We observed that the transcriptional patterns of the primary immune response is similar between species: Both genes belonging to the primary antiviral response (Hagai et al. 2018) and inflammatory genes (Liberzon et al. 2015) are mostly upregulated in monocytes in both mouse and *R. aegyptiacus*, with lower levels of upregulation of inflammatory genes in dendritic cells (DCs) and neutrophils. In contrast, IFN-stimulated genes (ISGs) (Shaw et al. 2017), upregulated during the secondary wave of response, are highly expressed in a range of different cell types in both species, and their relative levels differ between the species (Fig. 2c). Overall, this comparison between mouse and *R. aegyptiacus* suggests a conserved innate immune response across PBMC types in the initial stages of response to infection, followed by greater divergence in later stages. Importantly, type-I IFNs are almost exclusively upregulated in response to dsRNA and most highly in monocytes.

Induction of Different IFN Family Members is Restricted to a Monocyte Subset in Both *Rousettus aegyptiacus* and Mouse PBMCs

Next, we focused on the dynamics of the antiviral response across the *R. aegyptiacus* monocyte cell population, the most responsive cell type in our data, and the conservation of this dynamics in mouse. Among bat monocytes, we observed a cell cluster almost entirely composed of cells stimulated with dsRNA. Cells belonging to this cluster have high inflammatory and antiviral scores, suggesting a strong primary response (Figs. 1b and 2a). In addition, IFNB1, a major antiviral cytokine, is almost exclusively upregulated in this cluster. This monocyte subset (termed "IFN Monocytes") is also observed in mouse monocytes (supplementary fig. S2, Supplementary Material online). We next compared the three major cell states of *R. aegyptiacus* CD16 monocytes: The two groups of dsRNA-stimulated cells (IFN and non-IFN monocytes) and a third group with all remaining cells in unstimulated or mock-stimulated conditions. Using hierarchical clustering, we observed that the majority of genes upregulated in IFN monocytes, 263 out of 424 genes, are uniquely

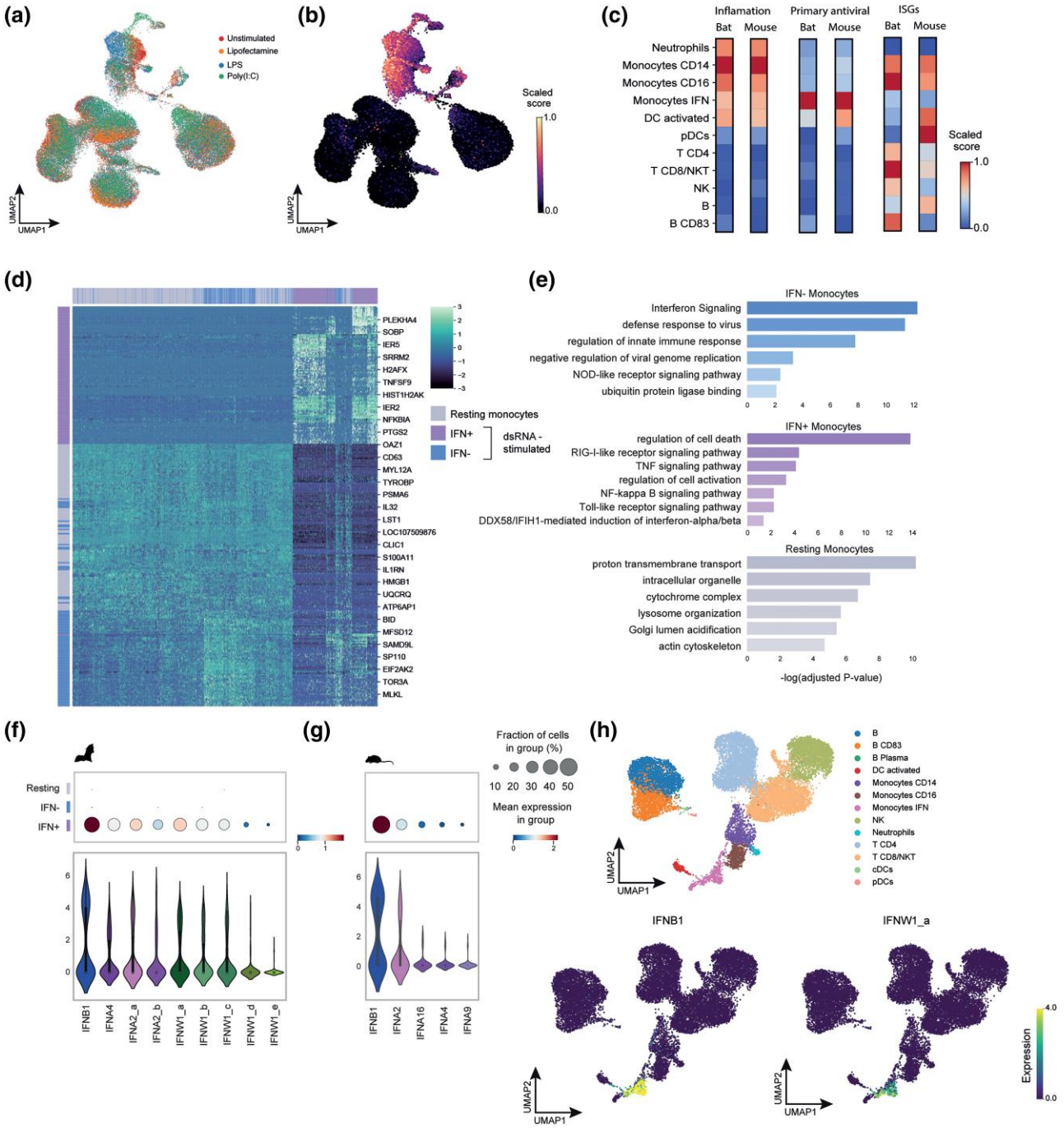

Fig. 2. Comparative analysis of PBMC transcriptional response to innate immune stimuli and IFN gene expression between *R. aegyptiacus* and mouse. a) UMAP of *R. aegyptiacus* PBMCs (five samples, $n = 59{,}443$ cells, as in Fig. 1b), cells colored by condition. b) UMAP of *R. aegyptiacus* PBMCs colored by inflammatory score, showing most inflammatory genes are upregulated in monocytes and DCs. c) Normalized expression scores of selected predefined sets of innate immune genes across different PBMCs in *R. aegyptiacus* and mouse: Inflammatory score, primary antiviral score, and Interferon-Stimulated Gene (ISG) score (see main text for details). Monocytes have the highest inflammatory and primary antiviral scores. d) Hierarchical clustering heatmap ("ward" as clustering method) showing expression of the three sets of state-DE genes from unstimulated monocytes and the two dsRNA-stimulated monocytes clusters (with and without IFN upregulation) in *R. aegyptiacus*. e) Enrichment analysis of state-DE genes, showing Gene Onthology (GO) terms unique for each of the three sets of genes (as in d). f) Top: Dot plots showing various type-I IFNs (IFNAs, IFNB1, and IFNWs) expression levels in *R. aegyptiacus* cells. Bottom: Violin plots showing the distribution of expression levels of various type-I IFNs across *R. aegyptiacus* IFN monocytes. IFNA2_a (LOC107511568), IFNA2_b (LOC107508426), IFNW1 a-e (LOC107518592, LOC107518590, LOC107518583, LOC107518588, and LOC107518582). g) As in f, in mouse monocytes. h) UMAP of dsRNA-stimulated PBMCs, colored by cell type (top), and showing the expression levels of IFNB1 and two of the IFNW duplicates in *R. aegyptiacus* (see the expression of additional type-I IFNs and similar analysis of mouse PBMCs in supplementary Data fig. S17, Supplementary Material online).

upregulated in this group and are not significantly expressed in other monocytes (Fig. 2d and "Materials and Methods"). In addition, hundreds of genes are downregulated in IFN monocytes in comparison with the other two states. Furthermore, the genes strongly upregulated in each of these three states are enriched in particular immune pathways and functions (Fig. 2e). The set of IFN monocytes upregulates genes related to cell death and to regulation of IFN induction. Importantly,

the set of IFN monocyte is also distinctive in its expression of an array of different type-I IFN genes as well as cytokines from other families.

We next asked whether the transcriptional patterns observed in the *R. aegyptiacus* IFN monocyte subset are also observed in corresponding mouse cells. We observed that indeed the mouse orthologs of genes uniquely upregulated in *R. aegyptiacus* IFN monocytes is also upregulated in a subset of mouse monocytes that express a range of IFNs and other cytokines. Similarly, the set of genes downregulated in *R. aegyptiacus* IFN monocytes is also downregulated in the analogous mouse cell cluster (supplementary fig. S16, Supplementary Material online). These findings suggest the induction of IFN genes that in *R. aegyptiacus* is limited to a small subset of cytokine-expressing monocytes, is similar to the induction patterns in mouse monocytes. These findings are also in agreement with studies of human blood and bone-marrow-derived monocytes, infected with various bacteria and with influenza (O'Neill et al. 2021; Avital et al. 2022), suggesting an overall conservation of IFN induction between *R. aegyptiacus* and other mammals.

Conservation of IFN Gene Induction Between *Rousettus aegyptiacus* and Mouse Cells Despite Numerous Events of IFN Gene Expansion and Loss

Type-I IFN gene families have undergone significant contraction and expansion during mammalian evolution. In *R. aegyptiacus* genome, there is a distinctively expanded set of IFN Omega (IFNW) duplicates (Pavlovich et al. 2018). In contrast, only a few copies of IFNA, another type-I IFN family with numerous copies in human and mouse genomes, are found in *R. aegyptiacus*. Given these genomic changes of IFN gene gain and loss, we asked (i) whether the different IFNW duplicates in *R. aegyptiacus* show transcriptional divergence between them in their response to dsRNA, and (ii) how the differences in copy numbers of various type-I IFNs between mouse and *R. aegyptiacus* are linked with the upregulation of IFN genes. We found a remarkably high degree of regulatory conservation between the two species: All type-I IFN genes are upregulated in monocytes rather than having diversified expression in different cell types. The strongest induced type-I IFN is IFNB1, with all other type-I IFNs co-expressed at lower levels compared to IFNB1 (Fig. 2f–h and supplementary fig. S17, Supplementary Material online).

Taken together, the above analyses show that: (i) Among PBMCs, monocytes are the strongest producers of IFNs. (ii) Within monocytes, IFNs are exclusively expressed in a small subset of cells that also upregulates an array of other cytokines while downregulating numerous other genes. (iii) IFNB1 is the strongest induced IFN gene. (iv) All other type-I IFNs, including recent duplicates in the lineages of mouse and *R. aegyptiacus*, are co-expressed with IFNB1 in the same cell subset, but in lower levels. These patterns of IFNs co-expressed in only a small set of cells were previously shown in different immune and nonimmune cells across primates and rodents, and were suggested to have evolved as a regulatory mechanism that balances rapid cytokine secretion while avoiding an excessive immune response (Hagai et al. 2018). Our results suggest that these transcriptional patterns, and likely also their underlying regulatory constraints, are also conserved in *R. aegyptiacus* cells.

Enterocyte Expression Dynamics During Maturation Along the Villus is Largely Conserved

Our previous analyses showed a conserved regulatory architecture of the IFN pathway in *R. aegyptiacus*. This was observed both at the cell-response level, with a subset of highly responsive monocytes that express a range of cytokines, and at the gene level, with IFNB1 being the most highly upregulated IFN.

Following this, we asked whether unlike the IFN pathway, other innate immune pathways show transcriptional divergence in barrier tissues between species that are primary sites of infection and expected to display patterns of divergence in innate immune genes. We first focused on the intestinal epithelium, a well-structured tissue, that its functions include mucus secretion, interactions with commensal microbiota and defense against pathogens (Peterson and Artis 2014; Allaire et al. 2018). Enterocytes, the most abundant cells in the epithelial layer, emerge in the crypt and migrate along the villus, until being shed off from the top of the villus a few days later (van der Flier and Clevers 2009). Enterocytes were shown to traverse a series of cell states, identified by distinct gene expression and related to different functions, during their migration from the crypt along the villus axis (Moor et al. 2018; James 2024) (Fig. 3a). Since enterocyte migration and maturation are well characterized in mouse and are also involved in the expression of innate immune genes in different stages of their maturation, they provide an excellent pathway to study the evolution of a dynamic cellular process involved in innate immune defenses in barrier tissues. Specifically, we asked whether the enterocyte region-dependent transcriptional programs, originally found in mouse SI, are conserved in the bat villus and whether divergence is related to innate immune genes.

For this, we first used genes previously found to be highly and specifically expressed in each of the five consecutive regions located from the bottom to the top of the mouse villus. These genes are termed zonation markers and their regions in mouse villus are denoted as v1 to v5 (Fig. 3a). Using the *R. aegyptiacus* spatial transcriptomics data, enabled us to test where the orthologs of these zonation markers are expressed along the villus in an unbiased manner: We observed a clear trend where the orthologous bat genes of these zonation markers tend to be spatially expressed from proximal to distal regions of the section, matching the expected patterns from mouse (Fig. 3b and d and supplementary figs. S14 and S18a, b, d, Supplementary Material online). This observation suggests a largely conserved gene expression dynamics along the villus in mouse and bat.

We then employed principal component analysis (PCA) of single-cell data from human, mouse and *R. aegyptiacus* enterocytes. The expression of zonation marker genes showed that PC1 captures the spatial bottom-to-top differentiation dynamics in each of the three species (Fig. 3c and supplementary fig. S18c and f, Supplementary Material online). This allowed us to use this axis to define enterocytes belonging to the bottom, intermediate, and top regions of the villus in mouse, human, and bat. When looking at individual gene expression along the PC1 axis, we observed that most of the zonation markers display expected transcriptional patterns (e.g. most bottom genes tend to be most highly expressed in the beginning of the PC1 axis in bat cells, Fig. 3e and supplementary fig. S18e, Supplementary Material online). However, we also observed specific genes that deviated from expected transcriptional

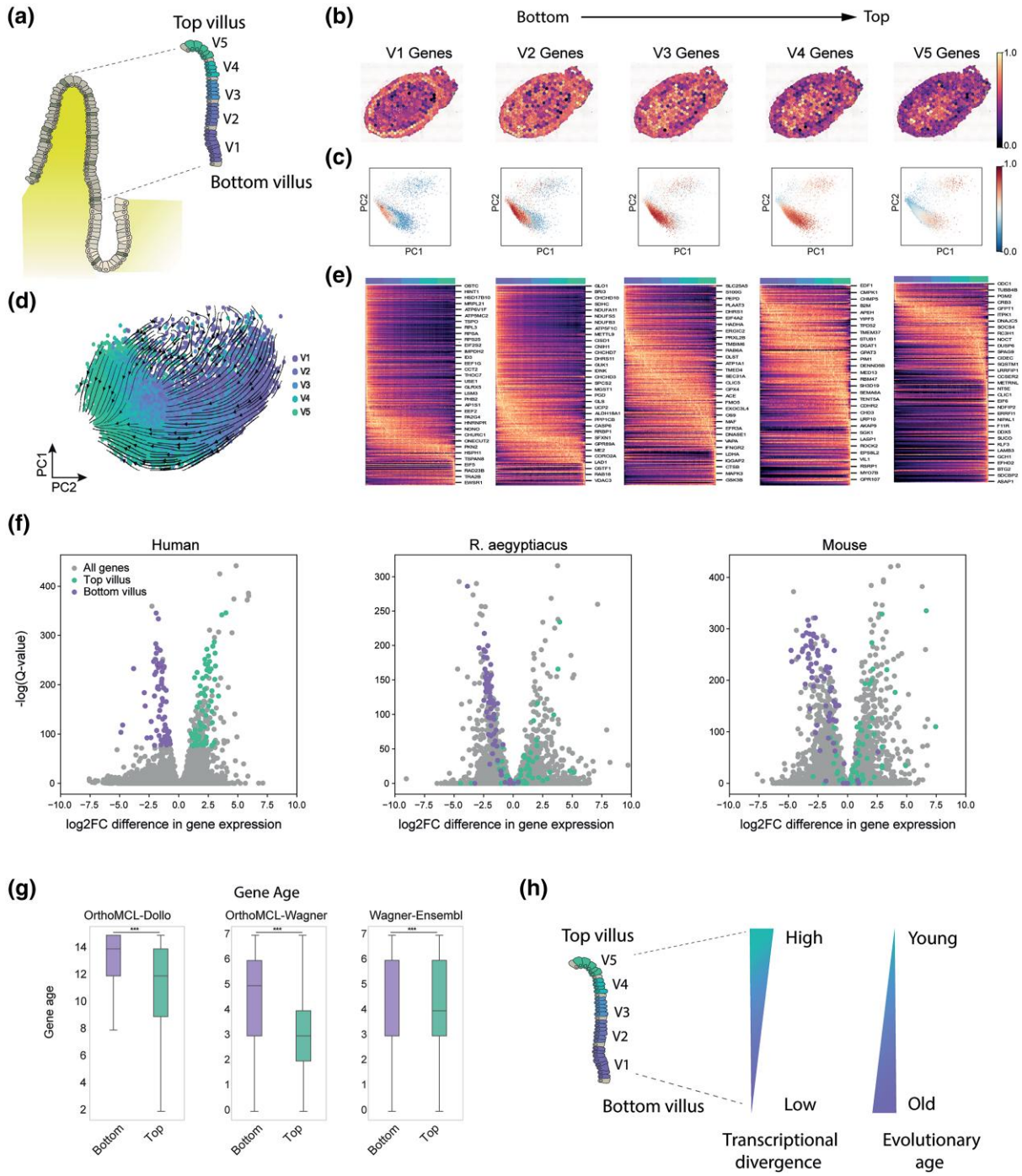

Fig. 3. Evolutionary analysis of enterocyte differentiation along the intestinal villus. a) Schematic of a transverse cross-section of the intestinal crypt and villus. The villus is partitioned into five consecutive bottom-to-top regions (denoted as v1 to v5). b) Scores of landmark gene expression (using mouse-to-*R. aegyptiacus* orthologs) from each of the bottom-to-top villus regions (v1 to v5) overlayed on a 10× Genomics Visium data of a *R. aegyptiacus* gut cross-section (additional samples are found in supplementary Data fig. S14d to f, Supplementary Material online). The analysis shows that gene expression along the villus axis (v1 to v5 genes) is similar between mouse and *R. aegyptiacus* enterocytes. Full gene lists appear in the GitHub link. c) PCAs of *R. aegyptiacus* enterocytes (based on single-cell data) overlayed with scores of bottom-to-top regions (v1 to v5). PC1 largely recapitulates bottom-to-top gene expression patterns. d) UMAP of *R. aegyptiacus* enterocytes colored by their inferred spatial localization along the tissues (v1 to v5) with dashed lines and arrows depicting inferred transcriptional trajectories as determined by scVelo. e) Heatmaps showing landmark gene expression in *R. aegyptiacus* enterocytes, each panel including a different set of regional genes (v1 to v5 regions, genes are based on mouse data (Moor et al. 2018). Cells are ordered based on PC1 axis, taken from c that denotes bottom-to-top villus localization. f) Volcano plots showing DE analysis of gene expression between top and bottom enterocytes in human, *R. aegyptiacus* and mouse. Human top genes are in green and human bottom genes are in purple—these are defined based on a DE analysis in human enterocytes. In the mouse and *R. aegyptiacus* volcano plots, we use the orthologs of the precomputed top and bottom human genes, and show the DE values of these ortholog genes in the respective species. Sets of top and bottom genes are matched by *q*-value in human. In mouse and *R. aegyptiacus* the orthologous bottom genes remain significant, while the orthologous top genes are less significant, suggesting that top genes are less conserved across species. g) Gene evolutionary age analysis of top and bottom genes (based on human genes and their age estimation using three different approaches, and taken from protein Historian). Age estimation distributions of bottom and top gene sets are compared using a one-sided Mann–Whitney test (***$P < 0.001$). High values denote old age. h) Schematic summary of evolutionary analysis of enterocyte differentiation along the villus: top landmark genes tend to be evolutionarily younger and transcriptionally divergent across species.

patterns between species, e.g. genes expected to be expressed mostly in the top villus region, are expressed in other regions of the bat villus.

In summary, the significant correspondence of zonation marker gene expression along the villus of the three studied mammals suggests an overall conservation of the bottom-to-top enterocyte expression programs. However, certain genes diverge in expression patterns between species and their characterization is the focus of the following section.

Top Villus Genes are Transcriptionally Divergent and Evolutionarily Younger Than Bottom Villus Genes

Following this, we quantified the transcriptional conservation of top versus bottom genes across species. For this, we performed a DE analysis between top and bottom enterocytes in each of the three species. We then compared the transcriptional divergence in top and bottom gene classes (after controlling for biases in DE values between the two sets of genes and focusing only on genes significantly expressed in all species). We observed that bottom genes are more transcriptionally conserved across species whereas top genes tend to be divergent. Thus, a gene highly expressed in the bottom villus region in one species is likely to be expressed in this region in other species, while top-expressed genes in one species tend to diverge in their transcriptional patterns across species (see the sets of top and bottom genes and their DE results overlayed across species in Fig. 3f and supplementary fig. S18g, Supplementary Material online). This greater divergence in later stages was also observed in other cell developmental pathways (Cardoso-Moreira et al. 2019; Murat et al. 2023).

Next, we compared the evolutionary age of the top and bottom villus genes, using several gene age estimations from ProteinHistorian (Capra et al. 2012). We observed that top villus genes are evolutionarily younger than bottom villus genes (Fig. 3g and supplementary fig. S18h, Supplementary Material online).

Finally, we asked which genes highly expressed in the top villus significantly diverge between *R. aegyptiacus* and the other two species. Interestingly, the most divergent genes in the top villus region are not involved in innate immunity. Instead, pathways enriched in these genes are associated with nutrient absorption, including in lipid transport and in anion binding (supplementary fig. S19, Supplementary Material online).

In summary, the dynamics of gene expression in enterocytes as they migrate along the villus is largely conserved across the studied mammals. As they migrate from the bottom to the top villus region, enterocytes become more transcriptionally divergent and express evolutionarily young genes, but this increased divergence does not involve innate immunity pathways (Fig. 3h).

Complement System Genes are Uniquely Expressed in *Rousettus aegyptiacus* Intestinal Epithelial Cells in the Crypt

In the above analysis, in contrast to our initial expectations, the transcriptional divergence observed in the top villus between species mostly involved genes unrelated to the innate immune pathways. We next asked whether transcriptional divergence is observed in the crypt—the region below the villus. Cells in the human crypt are known to secrete defensins, important antibacterial peptides (Lehrer and Lu 2012), but many defensin genes were lost through pseudogenization in bat genomes (Moreno Santillán et al. 2021), pointing to potential differences in innate immunity pathways in the bat's crypt. Using the DE analysis, where homologous gut cells were compared between species, we searched for genes more highly expressed in *R. aegyptiacus* in comparison with both human and mouse cells. We observed that both in stem cells and transit-amplifying (TA) cells, epithelial cells found in the crypt, central complement system genes are amongst the top DE genes in *R. aegyptiacus* in comparison to both human and mouse cells (supplementary tables S2 and S3, Supplementary Material online). These complement genes are strongly and uniquely expressed in these cells in bats but not in human and mouse cells. These patterns are observed in several other epithelial cell types (Fig. 4a–c; supplementary fig. S20, Supplementary Material online and supplementary tables S2 and S3, Supplementary Material online). Importantly, this expression is persistent across bat individuals and the fraction of cells expressing these genes within each cell type population is high (supplementary fig. S20, Supplementary Material online). This set includes genes encoding for both complement components (C3, C4, C5, C6, C7, and C9) and complement-associated proteases (C2, CFB, CFD, and CFI). Importantly, many genes of the membrane attack complex, a central immune effector and the final product of the complement cascade (Xie et al. 2020), including C5, C6, C7, and C9, are more highly expressed in *R. aegyptiacus* gut epithelia. CFI, an important protease that acts as a regulator of complement activation, is also more highly expressed in *R. aegyptiacus* cells than in both human and mouse. This pattern of higher expression of complement system genes in *R. aegyptiacus* epithelial cells is not observed in most nonepithelial cell types (supplementary fig. S20, Supplementary Material online). In agreement with this, when looking for pathways enriched in the top DE genes, we found many terms related to the complement system, including early and late stages of both the classical and the alternative pathways (see, for example, supplementary table S8, Supplementary Material online).

We then asked whether such transcriptional signatures of higher complement gene expression in bat cells also occur in other innate immune genes. However, comparison of the expression of a large set of genes from diverse innate immune pathways (taken from innateDB (Breuer et al. 2013), see supplementary table S9, Supplementary Material online) between *R. aegyptiacus*, mouse and human showed no such pattern in other pathways apart from the complement system (Fig. 4b). Next, we analyzed the spatial expression patterns of complement system genes across *R. aegyptiacus* gut. Using our single-cell data, where we can partition enterocytes to specific regions, based on our previous analysis, we observed that many of these genes tend to be expressed most highly in the crypt and then gradually decrease in expression along the villus (Fig. 4d). These observations were strengthened using the spatial transcriptomics data, where we clustered the spots into spatial regions (crypt, villus, and intestinal wall) (Fig. 4e), and estimated the expression of complement system genes in these regions (Fig. 4f–h and supplementary fig. S21a, Supplementary Material online, and supplementary fig. S21b, Supplementary Material online for comparison in mouse).

In summary, many genes from the complement system are uniquely expressed in *R. aegyptiacus* epithelial cells in comparison with human and mouse cells, and this expression is

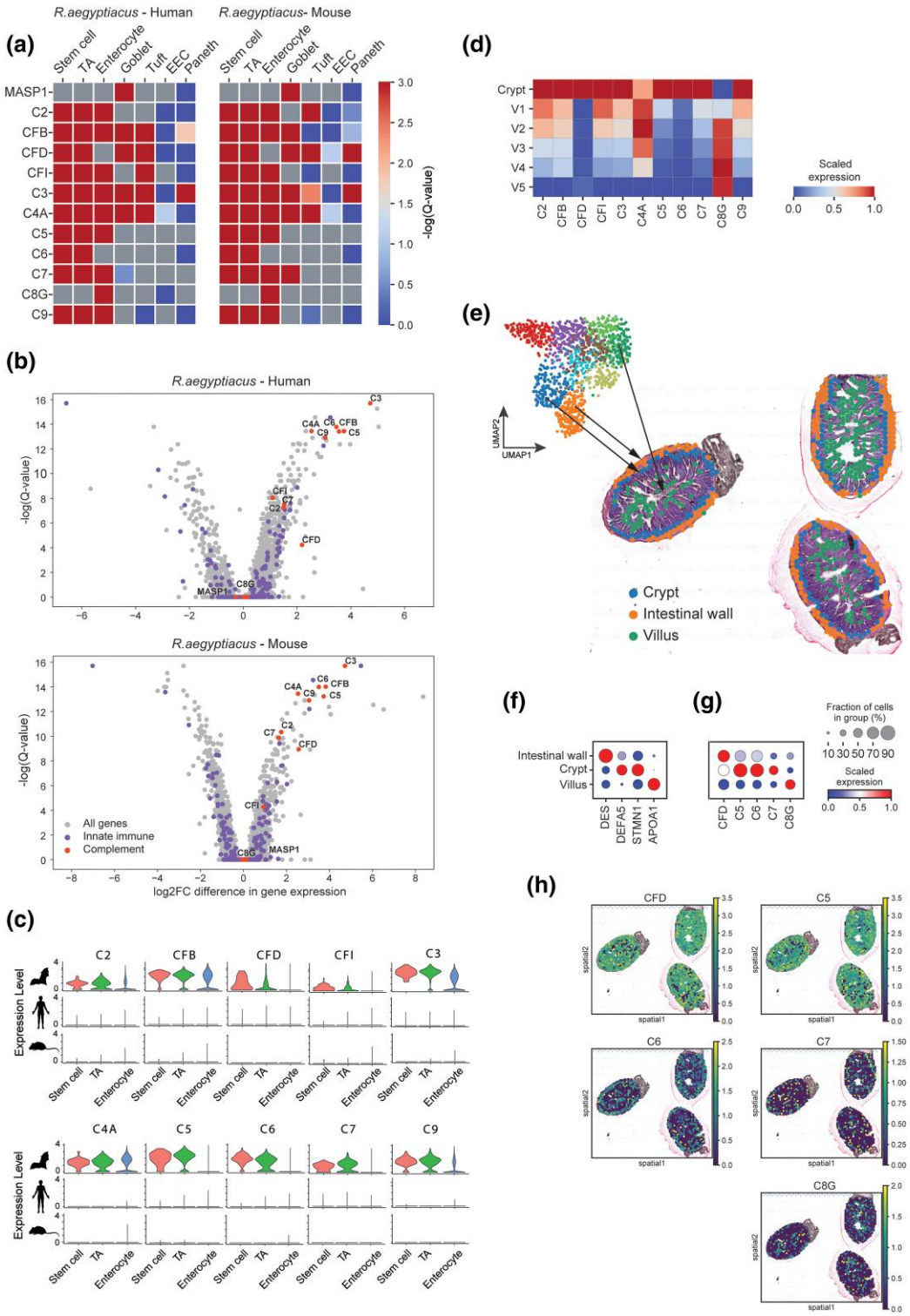

Fig. 4. Cross-species comparative analysis of complement system gene expression in epithelial cells in the intestine. a) Matrix plots showing DE results (–log[*Q*-value] between two species) of complement gene expression, between *R. aegyptiacus* and human (left) and *R. aegyptiacus* and mouse (right) homologous epithelial cells. Maximum values are trimmed at 3 (Q-value < 10^{-3}). In all cases of significant differences between species, the expression is higher in *R. aegyptiacus*, except for C2 in mouse Tuft cells, and for C8G in human enterocytes. b) Volcano plots showing DE analysis of gene expression between *R. aegyptiacus* and human (top) or mouse (bottom) epithelial stem cells. c) Violin plots of complement component and protease gene expression across different epithelial intestinal cell types in *R. aegyptiacus*, human, and mouse. d) Scaled expression levels of complement genes in the crypt (SC, TA, and Paneth cells) and along the five regions of the villus (v1 to v5 enterocytes) in *R. aegyptiacus* gut, using scRNA-Seq and localization based on Fig. 3c. e)–h) Analysis of complement gene expression using 10× Visium data: (e) Top: UMAP of grid spots from the *R. aegyptiacus* spatial transcriptomics data. Bottom: Localization of spots, colored by clusters from upper UMAP, in cross-sections of *R. aegyptiacus* gut, showing that the orange, blue, and green clusters refer to the intestinal wall, crypt and villus regions. f) and g) Dot plots showing relative expression in the three clusters that refer to different gut regions (as shown in e): f) known marker genes of these regions, and g) selected complement genes. h) Expression levels of selected complement genes across gut sections using spatial transcriptomics data (see all complement genes in supplementary fig. S22, Supplementary Material online).

strongest in the crypt for the majority of these genes. Other cell types and other innate immune genes do not show such strong and consistent transcriptional patterns.

Complement System Genes are Highly Expressed in *Rousettus aegyptiacus* Epithelial Lung Cells

Following our gut analysis, we asked whether similar signatures of complement system gene expression can be observed in epithelial cells in other barrier tissues in *R. aegyptiacus*. We chose to focus on lung, since it is a main site of infection and an important barrier to various pathogens, including SARS-Coronavirus-2. To investigate complement system gene expression in lung cells, we performed a DE analysis between lung homologous cell types (shown in Fig. 1c and supplementary fig. S5b, Supplementary Material online), contrasting orthologous gene expression between bat, human, and mouse. We again observed that a set of central complement system genes is more highly expressed in various *R. aegyptiacus* epithelial cells, including in basal, ciliated, club, goblet, from the airway epithelium, and, most prominently, in AT2 cells, from the alveoli (Fig. 5a and b and supplementary tables S4, S5 and S10, Supplementary Material online); (Raudvere et al. 2019). The expression of these complement genes was unique to *R. aegyptiacus* in most of these epithelial cell types in comparison with mouse and human cells, and included genes expressed in early stages of the classical pathway (C1S, C1R, C2 and C4A) and in the alternative pathway (CFB and CFD) (Fig. 5c and supplementary fig. S22, Supplementary Material online). Most late-stage genes of these pathways do not differ between species, with the exception of C9, which is higher in bat AT2 cells. The results regarding complement expression in human and mouse cells were corroborated by previous analyses of unrelated single-cell lung data (Chaudhary et al. 2022). The set of complement system genes more highly expressed in *R. aegyptiacus* lung epithelium overlaps with genes expressed more highly in *R. aegyptiacus* gut epithelium, but is not identical.

As in the gut epithelium, innate immune genes in general are not more highly expressed in bat lung cells in comparison with human or mouse cells (Fig. 5c). In addition, these expression patterns of complement system genes were not observed in most nonepithelial cell types in the lung. Thus, *R. aegyptiacus* epithelia of both the lung and the gut exhibit unique expression patterns of complement system genes.

Serum Levels and Coding Sequence Evolution of Complement System Genes in *Rousettus aegyptiacus*

The complement system is mostly known for its antimicrobial activities in the blood stream. Based on a previous genomic analysis, several other immune proteins secreted to the blood were suggested to have undergone significant evolutionary and functional changes in *R. aegyptiacus*, including short pentraxins (C-reactive protein and serum amyloid P component [SAP]) that are pseudogenes and nonfunctional (Larson et al. 2021). We thus sought to characterize the serum levels of various complement system proteins in *R. aegyptiacus*. We employed mass spectrometry-based proteomics to characterize serum proteomes of four bat and four mouse individuals. We detected almost all secreted complement system proteins, many of which were amongst the most abundant proteins found in both bat and mouse sera (Fig. 5d). Interestingly, some of the protein rankings differed between the two species—e.g. C9 was highly abundant in bat but not in mouse serum, while the opposite was observed in CFD serum levels. Importantly, these trends were consistently observed across the individuals tested in both species (supplementary fig. S23, Supplementary Material online). In general, our findings suggest that complement system proteins are among the highest in *R. aegyptiacus* serum, and that these relatively high levels are similar to those observed in mouse serum. We note that the differences observed in serum protein levels between the species may originate in environmental factors and differences in microbiome, despite the fact that these levels are similar between the four individuals within each species.

We next characterized the coding sequence evolution of the complement system genes, to determine whether these genes evolve rapidly in sequence. We employed a site model implemented in Phylogenetic Analysis by Maximum Likelihood (PAML) (Yang 2007) to test for positive selection in coding sequences of 14 complement system genes using orthologous genes from different bat species representative of the Chiroptera order. We observed that eight of the 14 genes tested show strong statistical evidence of positive selection (see supplementary table S11, Supplementary Material online). Taken together, we observed significant evolutionary changes in the *R. aegyptiacus* complement system genes, both in expression levels in lung and gut epithelia (Figs. 4 and 5a–c) as well as in coding sequences across bat species. Figure 5e summarizes these changes along the classical and alternative complement pathways. We elaborate on these findings in the wider context of evolution of secreted immune proteins in bats and mammals in "Discussion". Following the evolutionary and comparative expression analyses, we probed the activities of the *R. aegyptiacus* complement system. To this end, we employed a hemolytic activity assay of the bat complement system against rabbit blood (Fig. 5f). We observed a significant hemolytic activity in comparison to control, suggesting that bat complement system functions as expected, at least in terms of hemolysis.

Discussion

R. aegyptiacus is considered an important model for studying infection and immunity, due to its asymptomatic infection with Ebolavirus and Marburgvirus, two of the most lethal viruses to humans (Pavlovich et al. 2018; Wang et al. 2021). Previous studies, including by us, have investigated different mechanisms by which *R. aegyptiacus* immune system differs from the well-characterized immune systems of mouse and human (Kuzmin et al. 2017; Pavlovich et al. 2018; Guito et al. 2021; Larson et al. 2021; Schneor et al. 2023). Many of these studies pointed to potential adaptation through increased tolerance, where the immune response to infection is limited to avoid tissue damage. In contrast, molecular mechanisms that can give rise to increased resistance to disease, such as higher basal-level expression of innate immune genes, have not been previously described in *R. aegyptiacus*. These mechanisms can shorten the response time against invading pathogens, leading to a more effective and faster resolution of infection (Demian et al. 2024). To address this gap in studying immune resistance, we employed single-cell transcriptomics of *R. aegyptiacus* cells from two barrier tissues and of PBMCs, and studied them in a comparative manner to human and mouse cells. This allowed us to systematically compare immune gene expression between these species, and to find

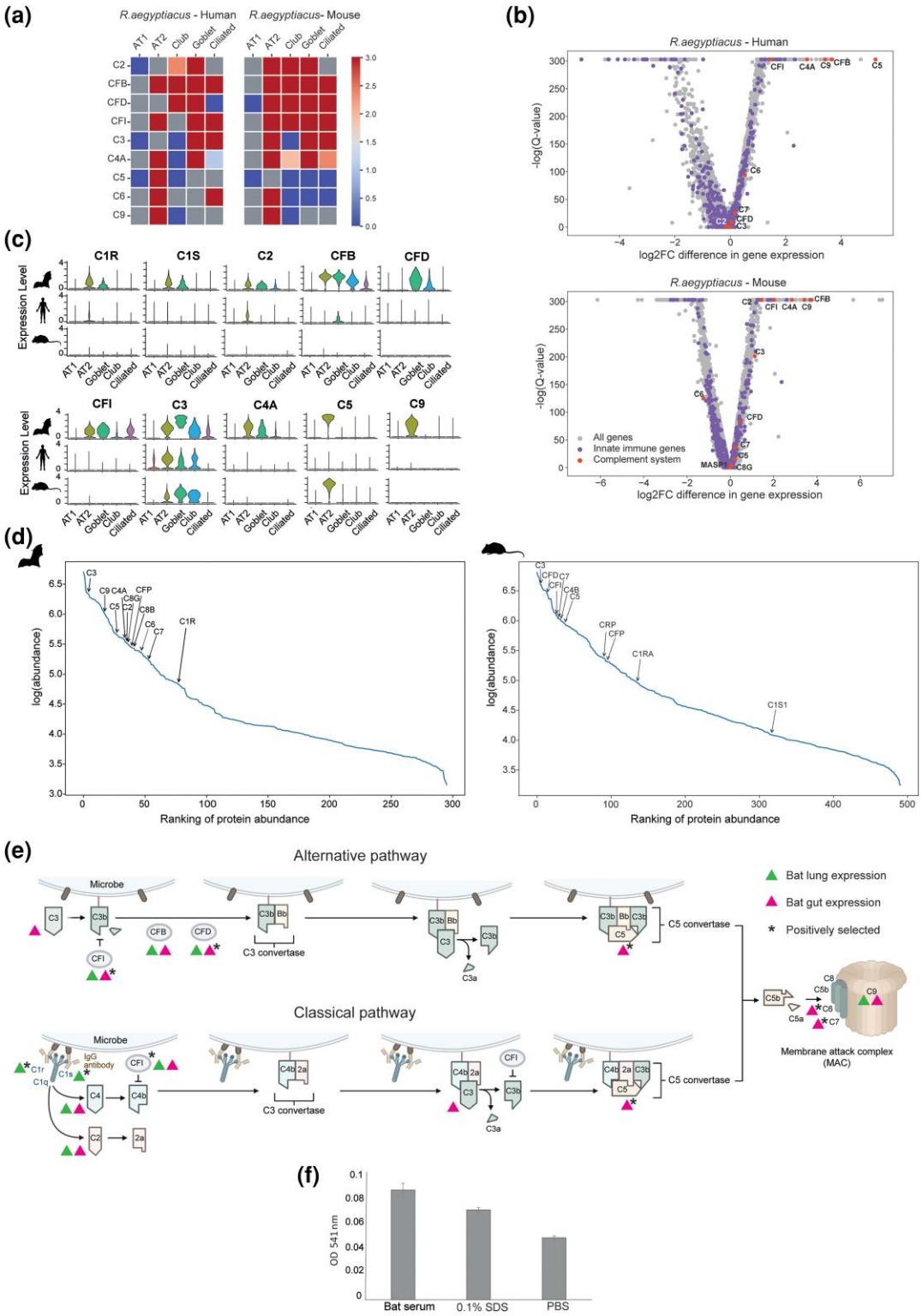

Fig. 5. Comparative analysis of the complement system in lung and serum and functional analyses. a) Matrix plots showing DE results (−log[*Q*-value] between two species) of complement system gene expression, between *R. aegyptiacus* and human (left) and *R. aegyptiacus* and mouse (right) homologous epithelial cells. Maximum values are trimmed at 3 (Q-value < 10^{-3}). In all cases of significant differences between species, the expression is higher in *R. aegyptiacus*, except for C6 expression that is higher in mouse AT2 and in human ciliated cells. b) Volcano plots showing DE analysis of gene expression between *R. aegyptiacus* and human (left) or mouse (right) AT2 cells. c) Violin plots of complement component and protease gene expression across different epithelial lung cell types in *R. aegyptiacus*, human and mouse. d) Serum protein abundance, based on Mass Spectrometry proteomics, in *R. aegyptiacus* and mouse. Complement system proteins are indicated. Proteins are ordered by relative rankings of their levels (x axis), computed as the mean of four individuals per species. e) Schematic representation of the complement pathway overlayed with several evolutionary analyses: Genes expressed uniquely in *R. aegyptiacus* gut and lung epithelial cells are marked in pink and green, respectively. Genes with signatures of positive selection across bat species are marked with an asterisk. C8A that is part of the C8 complex together with C8B and C8G, also displays signatures of positive selection. See supplementary Data table S11, Supplementary Material online for details. The figure was created in BioRender (2025) https://BioRender.com/h42d989. f) Hemolytic activity assay of *R. aegyptiacus* serum versus controls (0.1% SDS, Phosphate-Buffered Saline [PBS]) using rabbit blood. Hemolysis is shown as change in optical density (OD) at 541 nm (n = 4 individuals). Standard deviation is shown.

transcriptionally conserved and divergent immune-related pathways.

Starting with the IFN pathway, we studied both basal expression of IFN regulators, as well as the induction of type-I IFN genes in both mouse and *R. aegyptiacus* cells. We observe similar transcriptional patterns between these species in: (i) basal-level expression of genes related to IFN production, and in (ii) the induction of type-I IFN following dsRNA-stimulation. Our results show that after stimulation of PBMCs, type-I IFN production is almost exclusively observed in a subset of monocytes, and that these monocytes co-express many other cytokines and chemokines in both mouse and bat. These results are reminiscent of previous observations on human and mouse monocytes and macrophages infected by viruses and bacteria (O'Neill et al. 2021; Avital et al. 2022). This conserved pattern of cytokine upregulation in a small subset of cells suggests strong regulatory constraints imposed on cytokine expression, likely to avoid an excessive immune reaction and tissue damage (Hagai et al. 2018).

Interestingly, we find that rapid evolutionary expansion of type-I IFN genes in both the rodent and the bat lineages, does not result in transcriptional sub- or neo-functionalization of the lineage-specific IFN duplicates. Instead, these duplicates tend to be co-expressed with other IFNs in the same set of monocytes. Furthermore, these IFN duplicates are expressed in lower levels than IFNB1, a gene that exists as a single copy in both mouse and bat. Thus, the remarkable gene expansion and contraction of IFNs in the course of mammalian evolution is likely associated with coding sequence divergence that contributes to functional differences in binding of these IFN paralogs and in their downstream signaling (Levin et al. 2014). Indeed, a recent study showed that *R. aegyptiacus* cells stimulated by different IFNW subtypes display differences in inhibition efficiency of Marburgvirus replication (Pavlovich et al. 2020). Another possibility for these observations is that levels of different IFNs are fine-tuned with respect of their activity, such that IFNs with greater efficacy or with higher solubility, that can assist in eliciting the immune response in more remote locations, have lower expression levels. Interestingly, our findings differ from previous observations in a different fruit bat species, *P. alecto*, that found elevated levels of IFN genes and the IFN regulators IRF1, 3, and 7, in steady-state conditions (Zhou et al. 2014, 2016; Irving et al. 2020). These differences suggest how even seemingly close species of bats may have evolved different adaptive mechanisms against pathogens.

We next searched for innate immune genes that differ in expression between *R. aegyptiacus*, human and mouse in lung and gut, two important barrier tissues that act as main sites for pathogen infection. Steady-state expression of immune genes in barrier tissues can have important consequences for species ability to resist invading pathogens, since increased expression of such genes at central sites of infection can provide rapid means to inhibit pathogen replication. It is thought to be an important mechanism in the adaptation of different mammals to viral infection (Irving et al. 2020; Schneor et al. 2023). We found that in contrast to the majority of innate immune genes that do not significantly differ in steady-state expression between these species in either lung or gut cells, many complement system genes are strongly and uniquely expressed in bat epithelial cells in key regions from both tissues. Furthermore, we observed that complement system proteins are found in similar levels in serum of mouse and bat, highlighting the specificity of the transcriptional divergence observed in epithelial cells in barrier tissues. Interestingly, recent evolutionary analyses comparing bat genes with orthologs in other mammals found evidence for lineage-specific adaptation in coding sequences of bat complement system genes (Tian et al. 2023; Wu et al. 2023; Morales et al. 2025). In agreement with this, we found that a significant fraction of the complement system genes also show elevated evolutionary rates and signatures of positive selection in their coding sequences when compared across bat species. Taken together, our analyses point to concurrent evolutionary divergence in both sequence and expression of complement system genes in *R. aegyptiacus*.

We next employed functional assays to study the *R. aegyptiacus* complement system and found a significant hemolytic activity. In all, the combined evolutionary and functional analyses suggest that *R. aegyptiacus* possesses a functional complement system that significantly diverged in both expression patterns in key tissue regions and in coding sequence evolution. The expression of numerous components of the complement system in bat epithelia, together with the observed activity, may provide a mechanism to inhibit invading pathogens infecting these barrier tissues.

The multitude of differences observed in *R. aegyptiacus* complement system genes in comparison with other mammals in both sequence and expression, and the fact that the complement system functions as a cascade involving many proteins and protein complexes that act through different pathways and mechanisms, make it difficult to pinpoint how each of the observed evolutionary differences impacts the bat immune system to counteract various pathogens. Previous studies of several bat species found evidence for evolutionary and functional divergence in other immune pathways that, like the complement system, involve secretion of proteins. Some of the genes that belong to these pathways or their regulators, including defensins, pentraxins, ISG15 and several inflammatory cytokines, were either pseudogenized, inactivated or their expression levels were dampened in bat cells (Ahn et al. 2016, 2019; Larson et al. 2021; Moreno Santillán et al. 2021; Wu et al. 2023; Morales et al. 2025). Thus, the observed evolutionary divergence of the *R. aegyptiacus* complement system may be one of several adaptations of *R. aegyptiacus* to achieve a fine-tuned and effective immune response against pathogens.

Our analysis is limited by several factors: First, our comparison is between three species, one of which is an inbred mouse model. The individuals tested from each of these species had different past exposures to pathogens that may have affected the transcriptional patterns we observe. The lack of existing analogous data from other related species, and especially bats, limits our comparison and does not allow us to determine whether the unique transcriptional behavior of complement system genes observed in *R. aegyptiacus* epithelial cells, is characteristic to other bat species as well. Furthermore, while we hypothesized that this basal expression of complement system genes may be important for fending off invading pathogens, the functional consequences of these observations and whether this heightened basal expression is indeed adaptive remains to be tested. In a similar fashion, our observation that rapid IFN gene duplication is not linked with rapid transcriptional divergence, still leaves the possibility that different IFN paralogs are functionally divergent due to differential binding to, and activation of, the IFN receptor and its downstream signaling cascade. Finally, while

evolutionary changes in expression and in coding sequences can lead to increased resistance against certain pathogens, they may also entail costs in the form of increased sensitivity to other pathogens that infect bats (O'Shea et al. 2016; David et al. 2021; Weinberg et al. 2022), immune-related pathologies or metabolic costs.

In summary, our work provides a comprehensive analysis of gene expression in important tissues in *R. aegyptiacus* in comparison to mouse and human cells, coupled with immune stimulation and spatial analysis. It points to conserved immune pathways and, in stark contrast, finds that *R. aegyptiacus* complement system genes display significant transcriptional divergence in addition to rapid coding sequence evolution and a significant hemolytic activity. Characterization of the complement system function and evolution is particularly important given its potential association with COVID-19 pathogenesis (Zelek and Harrison 2023). Thus, in addition to providing an important resource for the community, our data and findings can also advance understanding of the mechanisms behind pathological immune conditions in humans.

Materials and Methods

Ethical Statement

Experimental protocols were approved by the Tel-Aviv University Animal Care and Use Committee (04-22-027, 04-21-065, and 04-20-023) according to the Israel Welfare Law (1994) and the National Research Council (*Guide for the Care and Use of Laboratory Animals*, 2010), and by the Israeli National Park Authority (2021/42760). Healthy adult male Egyptian fruit bats (*R. aegyptiacus*) were housed in our facilities in the Zoological Garden at Tel-Aviv University in a controlled environment and their health status was monitored for any sign of disease throughout this period by a specialized veterinarian. Healthy C57BL/6J adult male mice were obtained from the Tel-Aviv University animal facility (which is a conventional animal facility).

Experimental Procedures

All bats taken for these experiments were first examined for any clinical signs, then housed in our facility and monitored for a long period by a specialized veterinarian, ensuring that they are healthy, that they do not show any physiological or behavioral signs of disease, and that no bat with clinical symptoms is in contact with them, following our established protocols of monitoring their health status (Moreno et al. 2021; Costantini et al. 2022; Weinberg et al. 2022). We note that while this bat species is known to be infected asymptomatically with certain viruses, particularly from the *Filoviridae* family, these viruses are not endemic to the region where the individuals used in this study originate from.

Tissue dissociation was performed using protocols that were as similar as possible to protocols used in previous work on human tissues (Vieira Braga et al. 2019; Elmentaite et al. 2021; Stephenson et al. 2021). Cells mapped from these human tissue dissociations were used as comparisons to *R. aegyptiacus* and mouse cells in some of the analyses below.

Isolation of Gut Cells for Single-cell Transcriptomics

Gut tissue sections, specifically the lower part of the upper third intestinal tract, from eight bats were collected following transcardial perfusion with cold D-PBS (02-023-1A, Biological Industries). Samples were cleaned and then sliced longitudinally, cleaned, and again washed with D-PBS. Next, samples were minced and 0.15 to 0.2 g of the minced tissue was transferred into the digestion mix (1.07 wU/mL Liberase DH [Roche, 5401054001], [70 U/mL] Hyaluronidase [Sigma-Aldrich 385931-25KU], [70 ug/mL] DNAse I [11284932001, Roche] in Hanks' Balanced Salt Solution buffer [H6648, Sigma-Aldrich]). The samples were incubated for 25 min on a shaking platform at 150 rpm, and gently mixed every 10 min. Following incubation, the cells were passed through a 40 mM filter into a 50 mL falcon and added with 12 mL of Neutralization media (DMEM, Rhenium [41965039], 10% Heat inactivated Fetal Bovine Serum (FBS) [Rhenium, 10270106]). The cells were pelleted using centrifugation (400 G, 4 °C for 5 min), resuspended in DMEM and counted. Depending on red blood cell (RBC) presence in the pellet, samples were then treated with RBC cell lysis (Sigma, R7757) according to the manufacturer's protocol, quenched with 10% FBS in D-PBS, and again pelleted and resuspended. Dead-cell removal protocol (Biotec Miltenyi, 130-090-101) was applied according to the manufacturer's protocol in cases when cell viability was lower than 75%. The flowthrough was then pelleted at $400 \times g$ and resuspended in Phosphate-Buffered Saline (PBS) with 0.05% Bobine Serum Albumin (BSA). Cells were counted and loaded on the 10× Genomics Chromium instrument for single-cell library preparation, aiming to capture 10,000 cells, using 3′ v2 chemistry according to the manufacturer's protocol. Libraries were sequenced on an Illumina NovaSeq 6000 using the NovaSeq 6000 SP Reagent Kit v1.5 (100 cycles) to generate 84-bp paired end reads.

Mouse SI and colon samples (5 and 2, respectively) were processed in a similar manner. In the case of SI, we took samples from the jejuno-ileal region. In the case of colon, we took the whole colon. Incubation time with digestion mix was 25 min.

Preparation and Processing of Gut Sections for Spatial Transcriptomics

Gut sections were frozen in OCT according to 10× Genomics Visium protocol. Then 10× Genomics Visium protocol was applied on the (OCT)-embedded fresh frozen samples. All tissues were sectioned using a Leica CX3050S cryostat and were cut to obtain a 10 µm width. Samples were then tested for RNA integrity using a Tapestation 4200. Only blocks with RNA Integrity Number above 7 were used. Tissue optimization was performed, resulting in a permeabilization time of 23 min. The Visium spatial gene expression protocol from 10× Genomics was applied by loading a total of 11 gut sections from two individual bats onto the Library Preparation Slide (4 grid sections) and following the manufacturer's protocol. All images for this process were scanned at 40× with an Aperio Versa 200 slide scanner. Libraries were sequenced on an Illumina NovaSeq 6000 using the NovaSeq 6000 SP Reagent Kit v1.5 (100 cycles) to generate 84-bp paired end reads.

Isolation of Lung Cells for Single-cell Transcriptomics

Lung tissues of eight bats were removed following transcardial perfusion and washed in cold D-PBS (Biological Industries, 02-023-1A). Trachea was removed and the tissue was immediately injected with an enzyme mix based on previous work

(Vieira Braga et al. 2019) (Dispase II 50 caseinolytic µ/mL [Sigma-Aldrich, D4693], Elastase 4.3 µ/mL [Worthington Biochem, Worthington, LS002292], Dnase I 30 µg/mL [Roche], Collagenase A 2 mg/mL [Roche, 10103578001], $CaCl_2$ 5 Mm [Sigma]) followed by mincing and a brief incubation in a CO_2 incubator at 37 °C. Samples were then transferred to a shaker-incubator for 20 min at 37 °C, 150 rpm, followed by an immediate addition of 15 mL of neutralization buffer (DMEM [Biological industries 01-052-1], 10% FBS [Rhenium, 10270106]). Samples were then passed through a 40 um strainer twice and pelleted at 400 × *g*, 5 min at 4 °C. Samples were then treated with RBC cell lysis (Sigma, R7757C, according to the manufacturer's protocol) and quenched with (10% FBS, D-PBS). Cells were then pelleted at 400 × *g*, 5 min at 4 °C, resuspended in DMEM and counted. Dead-cell removal protocol (Miltney, 130-090-101) was applied according to manufacturer protocol in cases when cell viability was lower than 75%, and the flowthrough was pelleted at 400 × *g*, 5 min at 4 °C and resuspended in PBS with 0.05% BSA. Cells were counted and loaded on the 10× Genomics Chromium instrument for single-cell sequencing, aiming to capture 10,000 cells, using 3′ V2 chemistry, according to the manufacturer's protocol for CellPlex samples, or c_ChromiumNextGEMSingleCell 3′ v3.1_Rev D protocol for the standard protocol Libraries were sequenced on an Illumina NovaSeq 6000 using the NovaSeq 6000 SP Reagent Kit v1.5 (100 cycles) to generate 84-bp paired end reads.

In two cases, we tested an additional protocol: in one individual, we also tested the protocol without injection, and in another individual, we tested a cold dissociation protocol combining a similar digestion mix with an additional Bacillus Licheniformis protease—subtilisin A (Sigma, P5380). The procedure was performed as suggested in protocols.io (doi.org/10.17504/protocols.io.ymgfu3w).

For mouse lungs, we followed the same procedure we used for the majority of bat samples, with mouse lungs taken from three adult male individuals.

Isolation of PBMCs

R. aegyptiacus blood was collected from five individuals during transfusion and kept in heparinized tubes to prevent clot formation. PBMCs were isolated using 63% Percoll (Sigma, Cytiva; 17-0891-01) solution, according to standard density gradient centrifugation methods (30 min, 400 × *g*). Samples were then treated with RBC cell lysis (Sigma, R7757), quenched with 10% FBS in D-PBS, and again pelleted and resuspended.

In the case of mice, since the amount of blood from each individual is limited, we combined blood from several individuals (six and nine in two separate experiments) before continuing to PBMC isolation.

Cells were then counted and divided into 12-well plates with ~2×10^6 cells in each well. Cells were incubated overnight at 37 °C in medium (IMDM [Biological Industries], supplemented with 10% of heat inactivated FBS [Rhenium, 10270106], Penicillin–Streptomycin–Amphotericin-B [Biological Industries, 1 03-033-1C]).

Innate Immune Stimulation and Single-cell Profiling of PBMCs

With the collected PBMCs, we aimed to study the innate immune response, by stimulating them with two PAMPs—LPS and dsRNA that trigger antibacterial and antiviral response. These are conserved and well-characterized PAMPs that enable studying the unmodulated host innate immune response in a comparative manner across cells and species while avoiding host–pathogen-specific biases (Hagai et al. 2018). Furthermore, we were aiming to characterize the immediate response, following a short stimulation time, and collected the cells after 4 h of stimulation. This was done following a time course calibration we conducted on immune and nonimmune cells from various mammals, where we observed that 4 h is the optimal time point to achieve a strong transcriptional response without high levels of cell death and before additional processes, such as secondary feedback loops are activated in these cells (Hagai et al. 2018; Kumasaka et al. 2023; Schneor et al. 2023).

A day following collection and overnight resting, cells were either stimulated with LPS 100 ng/mL (Invivogen, tlrl-3pelps), 1 µg/mL high-molecular mass poly (I:C) (Invivogen, tlrl-pic), transfected with 2 µg/mL Lipofectamine 2000 (ThermoFisher, 11668027), and either mock-transfected or kept untreated. Following 4 h of incubation, stimulation was terminated by collecting the floating cells and trypsinizing (Trypsin 0.05%, no Ethylenediaminetetraacetic acid, Sartorius, 03-046-1B) the attached cells on the bottom of the well. Cells were then washed in 0.05% PBS. Next, cells were counted and loaded on the 10× Genomics Chromium instrument for single-cell sequencing, aiming to capture 10,000 cells. We used either 10× Genomics CG000390 Rev B protocol Chromium Single-Cell 3′ gene expression V.3.1 (10× Genomics) for CellPlex samples, or CG000204_ChromiumNextGEMSingleCell 3′ v3.1_Rev D protocol for the standard protocol. Libraries were sequenced on an Illumina NovaSeq 6000 using the NovaSeq 6000 SP Reagent Kit v1.5 (100 cycles) to generate 84-bp paired end reads.

Computational Analysis

Mapping of Single-cell RNA-seq Data

R. aegyptiacus and mouse single-cell libraries from raw sequencing data were mapped to existing genomes and converted into UMI count matrices using 10× Genomics Cell Ranger v6.0 (Zheng et al. 2017). Human data were downloaded from previous works of the Human Cell (Elmentaite et al. 2021; Stephenson et al. 2021; Madissoon et al. 2023). For *R. aegyptiacus* libraries, we used the bat1K genome assembly (Jebb et al. 2020), deposited at the NCBI website as mRouAeg1.p (https://www.ncbi.nlm.nih.gov/datasets/genome/GCF_014176215.1/). We tested it against a different genome annotation (Pavlovich et al. 2018), and chose the bat1K assembly since it gave a higher number of cells and allowed better identification and separation of cell types. Mouse libraries were mapped to ENSEMBL v92 mouse transcriptome (GRCm38.p6), the same ENSEMBL version as the version used in the human mapping. Cell Ranger filtered count matrices were used for downstream analysis.

Manual Annotation of *Rousettus aegyptiacus* Genes

The current *R. aegyptiacus* genome assembly contains genes with missing annotations (appearing as "LOC"). To augment the current assembly, we used gene orthology relationship with human and mouse genes, as inferred by our orthology mapping using the EggNOG mapper and its vertebrate database (v2.1.2) (see orthology mapping procedure below). In addition, we used online annotations found in the online

NCBI website: https://www.ncbi.nlm.nih.gov/genome/gdv/browser/genome/?id=GCF_014176215.1.

The above-mentioned genes were missing from the downloaded version. Manually annotated genes by us appear in the dataset as "gene_LOCi" where "LOCi" is the original identifier and "gene" is the added manual annotation. In cases where there are more than one *R. aegyptiacus* gene matching to an EggNOG entry (i.e. paralogs likely originating from a recent duplication), we added a suffix of "_P".

Comparative Analysis of Bat, Mouse, and Human Cells

Orthology Mapping Across Species

The basis for most comparative analyses in this work is a set of one-to-one orthologs between human, mouse and *R. aegyptiacus*. Otherwise, in cases where we study gene duplicates, we specifically mention it. We used orthology relationships for the relevant species by running EggNOG 5.0 mapping (Huerta-Cepas et al. 2019) using the *R. aegyptiacus*, human, and mouse coding DNA sequence annotations, with the assemblies mentioned above. Genes were considered one-to-one orthologs across the three species if they matched the same EggNOG gene name.

Integrated UMAPs Across Species

Cross-species UMAPs were based on (i) expression of one-to-one orthologs across the three species, as defined above, and (ii) cells belonging to the same annotated cell type shared across at least two species (i.e. cell populations that were not found in two of the three species were excluded from these integrated maps). In each such shared cell type, we down-sampled the cells to achieve an equal number of cells per cell type across the species. For integration between mouse and *R. aegyptiacus* we also removed cells with over 10% mitochondrial reads from both the species. We integrated the data using Seurat v4.1.1 integration pipeline. Each dataset were normalized using LogNoramalize. FindVariableFeatures was used for finding highly variable genes (HVGs) for the following stages. Canonical-Correlation Analysis (CCA) and Mutual Nearest Neighbours algorithms (Hao et al. 2021) were then used for batch correction before integrating the datasets with IntegrateData. The integrated data were then scaled and PCA dimensionality reduction was calculated based on HVGs (npcs = 30). RunUMAP (dim = 1:30), FindNeighbors (dim = 1:30), and FindClusters (resolution = 0.5) were then used for clustering and visualizing the integrated data. The integrated datasets were then visualized using Uniform Manifold Approximation and Projection (UMAP) (using R's DimPlot).

Correlation Between Cell Clusters Across Species

Cross-species comparisons were performed between *R. aegyptiacus* cells and human and mouse cells in each of the three tissues we studied. The cell types were compared in a pair-wise manner (*R. aegyptiacus*-human and *R. aegyptiacus*-mouse). In each case, gene expression in each cell cluster was aggregated to represent a "pseudo-bulk" gene expression of this cluster. Spearman's rank correlation between the expression levels of orthologous genes between cell clusters in *R. aegyptiacus* and the other species were then computed using differentially expressed (DE) genes, representing the marker genes that define each cell cluster and computed using Seurat v4.1.1 (Hao et al. 2021) FindMarkers. We compared either genes that are found to be DE genes between clusters in both species (the intersection of markers across the species), or the genes that are found to be DE genes between clusters in at least one of the species (the union of markers across the species). In each case we only used genes that are one-to-one orthologs between the two species. In each tissue, we showed the correlation values of both the intersection and union of marker genes between human—*R. aegyptiacus* and mouse—*R. aegyptiacus*.

Gut Analysis

Single-cell RNA-seq Quality Control and Processing

For QC and processing of the single-cell data, we used Pandas (v.1.2.3), NumPy (v.1.20.2), Annadata (v.0.7.8), ScanPy (Wolf et al. 2018) (1.8.1), and Python (v.3.9.2). Genes were filtered to include those expressed in more than three cells. Cells were filtered for more than 200 expressed genes and for <50% mitochondrial reads, to match with previous processing of human gut single-cell data (Elmentaite et al. 2021). For doublet removal, we first used Scrublet (v.0.2.3) (Wolock et al. 2019) with a cut-off of 0.25. For further doublet exclusion during the downstream processing, we searched for unexpected co-expression of canonical markers from different cell types. For example, cells co-expressing CD3E/CD3D (markers of T cells) and EpCAM or other epithelial markers, were excluded from further analysis. Gene expression for each cell was normalized (sc.pp.normalize_total) and log-transformed (sc.pp.log1p). Cell cycle score was calculated using the expression of 97 cell cycle genes [Dissecting the multicellular ecosystem of metastatic melanoma by single-cell RNA-seq (Tirosh et al. 2016)]. The percentage of mitochondrial reads and unique molecular identifiers (UMIs) were regressed (sc.pp.regress_out) before scaling the data. These procedures were performed for *R. aegyptiacus* gut and for mouse small and large intestine.

Clustering and Cell Type Identification

Integration and batch correction of datasets were performed using bbknn (v.1.5.1, neighbors = 2, metric="euclidean", n_pcs = 30, batch_key="Sample"). Dimensionality reduction and Leiden clustering (resolution 0.4 to 2) were performed, followed by cell lineages annotations. We used computationally derived marker gene expression for each cluster—DE genes (using sc.tl.rank_genes_groups, method = "wilcoxon"). In addition, we searched for known markers to further annotate our cell clusters, using a set of genes taken from previous studies (Elmentaite et al. 2021; Niec et al. 2022; Madissoon et al. 2023). To identify subsets and cell populations in greater resolution, we subclustered the data by lineages, and again performed batch correction and Leiden clustering in an iterative fashion.

***Rousettus aegyptiacus* Cells.** Epithelial cells were subdivided, based on markers (in brackets), into stem cells (LGR5, RGMB, and SLC12A2), TA (MKI67, TOP2A, and PCNA), enterocytes (APOA1, ALPI, and ANPEP), goblet (MUC2 and REG4), Paneth (DEFA5, TFF3, and GUCA2A), tuft (AVIL, TRPM5, and POU2F3), and enteroendocrine cells (EEC; CHGA, and CHGB). We also identified two separate clusters of enterocytes and goblet cells that we term PLK2, based on the expression of this gene in these two populations.

Mesenchymal cells were subdivided into fibroblasts (DCN, LUM, and PDGFRA), pericytes (NOTCH3 and PDGFRB), and smooth muscle cells (SMC; DES, ACTA2, and TAGLN), while myofibroblasts were identified by the

expression of ACTA2, TAGLN, and PDGFRA, yet lacked the SMC marker desmin (DES). Fibroblasts were further divided into two populations by the expression of either PI16 or ADAMDEC1. In addition, we identified glial cells (MPZ, CDH19, and PLP1), and mesothelial cells on the basis of LRRN4 and PRG4.

Endothelial cells (PECAM1) were subdivided into vascular on the basis of VWF gene expression or lymphatic (LEC) on the basis of CCL21, PROX1, and LYVE1.

Myeloid cells were subdivided into monocytes (F13A1 and IL1B), macrophages (C1QA and CD163) and DCs. DCs were defined as either cDC1 (CLEC9A and XCR1) or cDC2 (IL18 and SIRPA), both expressing BATF3 and HLA-DRA, or as pDCs, on the basis of IRF8 and TCF4. Neutrophils (CSF3R, CCRL2, and G0S2), Mast cells (GATA2, IL1RL1, and MS4A2), and Eosinophils (PRG3, RFLNB, and CD24) were identified as well, comprising the granulocytes group.

Lymphocyte cells were subdivided into T/natural killer (NK) cells and B cells. The T cell (CD3D) compartment is composed of CD4 T cells, expressing CD4 and not CD8A, and vice versa for CD8 T cells, as well as an additional T CD8 subset, expressing GZMK. NK cells were identified based on the expression of NCR1 and KIR receptors (KLRB1 and KLRD1), yet lacking the expression of CD3D. Natural killer T (NKT) cells were identified by the expression of the KIR receptors together with CD3D and the lack of NCR1. Innate lymphoid cells (ILCs; TRDC) were defined as ILC3 (IL23R, KIT, RORC, FCER1G [An in vitro model of innate lymphoid cell function and differentiation]) or ILC2 based on the lack of ILC3 markers combined with a stronger expression of GATA3 and RORA. Cycling T cells were also identified, expressing CD3D together with STMN1. B cells were identified by the expression of CD79B together with MS4A1 while plasma B cells were expressing MZB1 as well. Cycling B and plasma cells were identified by the additional expression of STMN1.

Mouse Cells. We used the same markers as above, with the following differences:

In SI: SCs—we also used OLFM4, Enterocytes—ALDOB, RBP2, goblet cells—TFF3, SPINK4, Paneth—DEFA24, LYZ1, Tuft—DCLK1, Mesenchymal—CD34, COL6A2. In the immune compartment, additional markers were used for macrophages—LYZ2, H2-EB1, cDC2—CD209A, pDC—SIGLECH, BST2. In lymphocytes, CD28 was used for CD4 T cells and JCHAIN for B plasma cells.

In colon: In addition to the mouse SI markers and the *R. aegyptiacus* gut markers: Colonocytes were defined by the expression of CAR1, CAR4, and AQP8 and vascular endothelial cells by the additional marker SOX17. In the immune compartment, we also used the marker CCR2 for Neutrophils, for activated DC—CCR7 and FSCN1, and for CD4 T cells—LEF1.

Spatial Transcriptomics Mapping, QC and Spatial Abundance of Cell Type Analysis

Binary Base Call files were converted to fastq format and demultiplexed using 10× Genomics Space Ranger 2.0.0 (https://support.10xgenomics.com). The converted fastq files were then mapped to the reference *R. aegyptiacus* transcriptome (the same as with the single-cell RNA-seq data) using Space Ranger. Next, we spatially mapped gut cell types using our *R. aegyptiacus* spatial transcriptomics data, integrating scRNA-seq using Cell2location (v0.1) (Kleshchevnikov et al. 2022). Only Visium spots aligned on the tissue were used for analysis, exclusion of spots was performed with Loupe Browser v6.3.0. We employed the Cell2location model to estimate the abundance of each cell population in each spot. This model leverages the transcriptional signatures of reference cell types to decompose the mRNA counts in the 10× Genomics Visium data. The gene expression matrix was filtered to remove lowly expressed genes using filter_genes with default values. Cell2location was employed to estimate reference gene expression signatures of cell types from using negative binomial regression. For the processing of the 10× Visium data, we adjusted the hyperparameters in Cell2location as follows: The model was trained for 30,000 iterations; The RNA detection sensitivity, detection alpha, was set to 20 and the number of cells per location to 18, based on comparison with histology images paired with 10× Genomics Visium. In this analysis we used libraries from Scanpy (v1.8.1) (Wolf et al. 2018), Anndata (v0.8.0), and Matplotlib (v3.6.2).

For mouse SI spatial transcriptomics data, we used data from a previous study (Niec et al. 2022). We processed the mouse data as described above.

Transcriptional Analysis of SI Versus Colon Analysis

To establish a set of SI enterocyte and colonocyte signature genes, a DE analysis was performed between the two cell types in human and, separately, on mouse, using 1:1 orthologs across human, mouse, and bat. Enterocytes and colonocytes from mouse and human single-cell data (healthy adult samples) were down-sampled for equal cell numbers in each species (python random package with sample method, seed = 1), 4,271 of each type in human and 4,456 in mouse. Human enterocytes of duodenal and rectal origins were excluded, as well as pediatric samples. sc.tl.rank_genes_groups (method = "wilcoxon") was then used for DE analysis between enterocytes and colonocytes in each species. Genes were filtered for 0.01 adjusted *P*-value; mitochondrial genes were excluded from the analysis. From the DE results, we obtained 100 signature genes that are highly expressed in enterocytes versus colonocytes and vice versa. This was done by taking the genes with the lowest "Max Q-value" (the higher adjusted *P*-value of a gene in the enterocytes–colonocytes DE analysis in human and mouse).

For heatmap representation of enterocyte and colonocyte genes in different gut sections and in different species, we down-sampled the cells (human and mouse SI enterocytes and colonocytes and *R. aegyptiacus* enterocytes) to reach an equal number of 4,280 cells. Data were then normalized (sc.pp.normalize_total) and log-transformed (sc.pp.log1p) following the regression of mitochondrial reads and UMIs (sc.pp.regress_out) before scaling the data (sc.pp.scale). The data were plotted using sc.pl.heatmap. To test for relative gene expression of enterocyte and colonocyte signature genes in *R. aegyptiacus* enterocytes, *we used* a one-sided Mann–Whitney *U* test (scipy.stats.mann–whitneyu).

Evolutionary Analysis of Enterocyte Trans-differentiation Along the Villus

Top and Bottom Villus Scores

To identify the likely zonation of enterocytes in our single-cell and spatial transcriptomics data, we used five sets of landmark genes, highly expressed in specific regions along the villus, from a previous work that identified them in mouse villi using laser capture microdissection of five sequential regions along

the villus and bulk-RNA-seq (Moor et al. 2018). We then used only those genes that were identified as one-to-one orthologs across human, mouse, and bat. The scoring was done using sc.tl.score_genes() function with default parameters to calculate the average expression of selected genes subtracted with the average expression of a reference set of genes. The score was then standardized between 0 and 1. To visualize these scores in the spatial data, we used sc.pl.spatial.

Inferences of Enterocyte Zonation Along the Villus

Following the scoring, enterocyte single-cell datasets from each of the three species were filtered for genes expressed in more than three enterocytes, and then normalized (sc.pp.normalize_total) and log-transformed (sc.pp.log1p), following by regressing out mitochondrial reads and UMIs (sc.pp.regress_out). Log-normalized counts of HVGs were scaled (sc.pp.scale) before performing PCA. We then plotted the five zonation scores in human, mouse, and bat enterocytes. Since the scores largely followed PC1, we used PC1 coordinates to define enterocyte zonation, by dividing the cells into five sequential sections along PC1. For top versus bottom comparison, we further used 15% of the enterocytes found in the two extremes of the axis.

scVelo Trajectory Analysis

The cell trajectory analysis for the bat and mouse enterocytes was carried out with scVelo 0.2.4 (Bergen et al. 2020) package, as implemented in scanpy. Preprocessing of the enterocyte data were performed with the function scv.pp.filter_and_normalize (min_shared_counts = 20), followed by scv.pp.moments function. Gene-specific velocities were determined using scv.tl.velocity (mode = "stochastic") and scv.tl.velocity_graph(), by quantifying the steady-state equilibrium deviation from a ratio between unspliced to spliced mRNA levels. Gene-specific velocities were visualized with scv.pl.velocity_embedding_stream (basis = "pca").

In order to plot heatmaps of expression along the villus, a dynamic model pipeline was used with the functions scv.tl.recover_dynamics() followed by scv.tl.velocity (mode = "dynamic59al") and scv.tl.velocity_graph(). Heatmaps were plotted using scv.pl.heatmap for the five sets of gene signatures along the sections of the villus used for the enterocyte scores. Enterocytes were sorted by the PC1 coordinates used to identify the regions along the villus axis from which they likely originated.

DE analysis of top and bottom villi enterocytes

Top and bottom enterocytes were down-sampled (python random package with sample method, seed = 1) for equal cell numbers between regions and between species resulting in a total number of 627 enterocytes in each group. Downstream processing was performed in a similar manner as above ("Inferences of enterocyte zonation along the villus"), with the addition of a batch correction performed with bbknn (v.1.5.1, neighbors = 2, metric = "euclidean", n_pcs = 30, batch_key = "Sample" or "sample name"), and a UMAP dimensional reduction. DE analysis was carried out using sc.tl.rank_genes_groups (method = "wilcoxon") for each species individually between the top and bottom regions. Genes were annotated as top (positive logFC) or bottom (negative logFC) in each species separately. In addition, genes were labeled based on expression levels as: not expressed, expressed in more or <5% of the population, or expressed in more than 20% of the population.

Gene age

For the gene age analysis, we used genes expressed in more than 20% of the human enterocytes and based the analysis on the human DE analysis. We used human, as gene age estimations are available and best characterized for the human genome (although these one-to-one orthologous genes should not vary between species). For this, human enterocyte single-cell data were filtered for genes expressed in over 20% of the top or bottom enterocyte population by sc.pp.filter_genes (human, min_cells = int(0.2*human.shape[0])), then processed in a similar manner as for the DE analysis of the three species. 500 top (positive logFC) and 500 bottom (negative logFC) most significant genes were selected for the analysis by lowest adjusted *P*-value. Gene age estimations according to three different methods and family reconstruction (Wagner/Ensembl, Wagner/OrthoMCL, and Dollo/OrthoMCL) were obtained from ProteinHistorian (Capra et al. 2012). For each gene, age was defined with respect to the species tree, where a gene's age corresponds to the branch in which its family is estimated to have appeared (thus, larger numbers indicate evolutionarily older genes). Data were plotted using Seaborn package boxplot, for statistics we used a one-sided Mann–Whitney *U* test (scipy.stats.mann–whitneyu).

Transcriptional Conservation of Top and Bottom Genes

To study the transcriptional conservation of the sets of top and bottom genes, we compared DE results between top and bottom genes in human data with those in mouse and *R. aegyptiacus*. Human DE results were selected as the reference for comparison since its DE genes were the most significant (top versus bottom genes) and since it was also used in the gene age estimates. For comparison across species, we used two unbiased sets of top and bottom genes, where we controlled for the adjusted *P*-values, such that both sets would have a similar distribution of these *P*-values. For this, we used a function we developed previously (Fraimovitch and Hagai 2023): row_matchers.one_to_one_matches (col = −log Qval_human, eps = 5). We used this script with initial sets of 250 most significant genes from each of the bottom and top gene sets. This method yielded 70 human-paired DE genes (70 top and 70 bottom genes). Top and bottom genes were then projected on the bat and mouse DE data, to test the distributions of adjusted *P*-values of these two gene sets in each of these species. Data were visualized and statistical significance was determined as described above ("gene age") and the statistics as well, except for the Mann–Whitney *U* test performed for the human DE paired genes that were done as a two-sided test in order to check for biases in both directions. For volcano plot visualization, we used seaborn scatterplot with the DE analysis data.

Species-specific Top Gene Analysis

In this analysis we first searched for genes that are transcriptionally divergent such that they are either expressed as top villus genes only in the bat cells (in comparison with both human and mouse) or the opposite (i.e.—top genes in both human and mouse, but not in bat). We defined genes to be expressed as top in bat but not in human and mouse as follows: We first kept genes that are top in bat cells with an adjusted *P*-value < 0.01 and that their logFC in the other two species is below 0.5. We also asked that the difference between the logFC values

of bat versus either human or mouse will be positive. We then took the top 100 genes that are most significant in terms of having the highest differences of logFC in bats in comparison with either species.

For genes that are top in human and mouse but not in bat, we performed a similar procedure, where we used genes that (i) had an adjusted *P*-value < 0.01 in both human and mouse cells, (ii) their logFC in bat cells was below 0.5, and (iii) the differences between the logFC values of bat versus both human or mouse was negative. In each set, we searched for significantly enriched pathways and functions using g:Profiler (Raudvere et al. 2019) with the top 100 genes.

Expression Analysis Along the Villus of Specific Sets of Genes

In this analysis, we used one-to-one orthologous genes, found in gene sets with known functions. These sets were either the result of the previous analysis (see above—the two sets were those related to the terms: (i) Lipid transport Gene Onthology (GO): 0006869, and (ii) Anion binding GO:0043168) or involved in nutrient absorption and transport and taken from a previous study (doi.org/10.1084/jem.20191130). We only used genes expressed in each of the species in more than 10% of the enterocytes in at least one of the five regions along the villus. Expression was then visualized by sc.pl.matrixplot (standard_scale = "var") across the villi axis with the groups V1 to V5.

DE Analysis of Gut Cells Across Species

DE analysis was performed between homologous cell types in *R. aegyptiacus gut* and human or mouse SI as integrated Seurat objects using FindMarkers() of Seurat v3 with default parameters (min.pct = 10, logfc.threshold = 0.25, assay = "RNA"). This analysis included only those genes that were identified as one-to-one orthologs across human, mouse, and *R. aegyptiacus* and equivalent cell types were down-sampled (python random package with sample method, seed = 1) for equal cell numbers between the *R. aegyptiacus* and the other species. We later searched for significantly enriched pathways and functions using g:Profiler (Raudvere et al. 2019) with the top 50 significant genes (adjusted *P*-value < 0.01) with the highest logFC (see enriched pathways for R. *aegyptiacus* stem cells in supplementary table S8, Supplementary Material online).

The complement system gene set used in the analysis was taken from a previous work (Chaudhary et al. 2022) and is composed of pattern recognition, proteases, complement components, receptors, and regulators from all three major pathways. In order to visualize the DE results regarding complement system proteases and components we used seaborn's heatmap with −log (adjusted *P*-value) values, and set a maximum threshold of 3. Only significant DE genes (default FindMarkers() parameters) in at least one cell type in either *R. aegyptiacus*—mouse DE or *R. aegyptiacus*—human DE analysis were included. For visualization of the expression of the complement system genes in all three species, we used Seurat's (VlnPlot()) and dotplot(DotPlot()), with normalized log-transformed single-cell data.

For volcano plot visualization, we used seaborn's scatterplot with DE analysis data of all orthologs shared between the three species using Seurat v3′ FindMarkers with no threshold. The set of innate immune genes was obtained from InnateDB (Breuer et al. 2013).

Spatial Analysis of Complement Gene Expression

Spatial complement gene expression analysis was carried out using ScanPy in the following manner: Spatial transcriptomics data was normalized, log-transformed and scaled, similarly to the single-cell data analysis. Next, dimension reduction was performed followed by Leiden clustering (resolution = 1.4). The clusters were visualized by UMAP and on the spatial grid. Selected clusters were then annotated for either the intestinal wall, the crypt or the villus, based on markers of the cells residing in these areas as follows: Wall: SMC—DES, Crypt: Paneth cells—DEFA5 and STMN1 (a marker expressed in cycling and differentiating cells), Villus: Enterocytes—APOA1. Following annotation, DE analyses were performed using rank_genes_groups (method = "wilcoxon", group_by = "area") and selected complement components and proteases gene expression were visualized on the spatial grid or using ScanPy's dotplot.

In order to visualize the expression of the complement components and proteases along the villus, crypt cells (TA, Stem, and Paneth cells) and enterocytes were plotted for expression using ScanPy's matrix plot (sacpny.pl.matrixplot()) as was done in the top and bottom analysis section with single-cell data.

Lung Analysis

Single-cell RNA-seq Quality Control, Clustering and Cell Type Identification

For QC and clustering of *R. aegyptiacus* and mouse lung single-cell data, we employed a similar approach to the approach described above for gut cells, with the exception of using a threshold of cells with fewer than 30% mitochondrial reads.

Clustering and Cell Type Identification

R. aegyptiacus data were integrated and Leiden-clustered as described in the gut section. Clusters and subclustres were identified using computationally derived marker genes between clusters. We also used known markers from previous studies, as follows.

Rousettus aegyptiacus Cells. Epithelial cells were subdivided into Alveolar type-I (AT1; AGER, CLIC5, and RTKN2), Alveolar type-I (AT2; SFTPC, SFTPB, and MUC1), basal (KRT5, TP63, and KRT17), ciliated (FOXJ1 and DYNLRB2), club (SCGB3A2), and goblet cells (TFF3, MUC5AC, SPDEFF, and FOXA3). Tuft cells, also known as brush cells, were identified on the basis of BIK, PLCG2, ALOX5AP, and SOX9 (Strine and Wilen 2022).

Endothelial cells (PECAM1) were subdivided into vascular (VWF) and LEC (CCL21, MMRN1, and PROX1) cells. The vascular endothelial cells were further divided into capillary (EDNRB, CA4, TBX2, and PRX), venous (ACKR1 and VWF) and arterial on the basis of EFNB2, SEMA3G, and VWF (Schupp et al. 2021).

Mesenchymal cells were subdivided into fibroblasts (DCN, LUM, and PDGFRA), pericytes (NOTCH3 and PDGFRB), and SMCs based on the expression of ACTA2, MYH11, and DES. Fibroblasts were further divided into alveolar (COL13A1 and NPNT), adventitial (PI16 and COL1A1) and peribronchial (HHIP, FGF18, and WIF1) (Tsukui et al. 2020). Pericytes were divided into two populations based on the expression of ACTA2 in one of the subsets. In addition, we identified mesothelial cells on the basis of LRRN4, PRG4, and MSLN.

Myeloid cells were subdivided into CD14 monocytes (CD14, F13A1, and VCAN), CD16 monocytes (FCGR3A and CX3CR1), macrophages (CD163), and DCs. Macrophages were divided into alveolar macrophages, on the basis of MARCO, and to macrophages interstitial, based on a stronger expression of C1QA combined with a lack of MARCO expression. DCs were defined as either cDC1 (CLEC9A and XCR1), cDC2 (IL18), or activated DC (LAMP3, FSCN1, and CCR7), all expressing HLA-DRA as well as BATF3, and pDCs (IRF8 and TCF4). Neutrophils (CSF3R, CCRL2, G0S2, and S100A8), mast cells (GATA2, IL1RL1, and MS4A2), and eosinophils (PRG3, RFLNB, and CD24) were identified as well, comprising the granulocytes group. Neutrophils were further subdivided into subtypes based on the expression of OLFM4 (Clemmensen et al. 2012).

Lymphocytes were subdivided into T/NK cells and B cells. The T/NK population was subdivided into T (CD3) CD4 or CD8 expressing cells, ILCs and NK cells. The CD4-expressing T cells were further divided into naïve T cells on the basis of CCR7, TCF7, and LEF1, central memory CD4 (CM) T cells, a population with a weaker expression of these genes and effector memory (EM) CD4 T cells, on the basis of CXCR6 and CCL5. The CD8-expressing T cells were divided into CM and EM CD8 T on the basis of additional expression of GZMB and TBX21 (Bieberich et al. 2021), and NKT. NKT and NK cells were identified based on the expression of the KIR receptors KLRB1, KLRD1, and NCR1 and distinguished based on the expression of CD3D and CD3G (NKT), or lack of such expression (NK cells). ILCs (TRDC) were defined as ILC2, based on GATA3, MAF, and IL1RL1 expression, or as ILC3, based on RORC, IL23R, KIT, and FCER1G expression (Allan et al. 2015). Cycling T cells were identified by the expression of CD3D together with STMN1. B cells were identified by the expression of CD79B together with MS4A1, while B plasma cells were expressing MZB1 and JCHAIN. Cycling B and cycling B Plasma cells were defined based on the additional expression of STMN1.

Erythrocytes were also identified, using HBB and ALAS2 expression.

Mouse Cells. We used the same markers as above, with the following differences:

For goblet cells we used the marker MUC5B (Travaglini et al. 2020). For arterial endothelial cells, we used SOX17 (Schupp et al. 2021), and for the peribronchial fibroblasts we used ASPN as well (Tsukui et al. 2020).

In the immune compartment we used additional markers as follows: Mast cells—CPA3, classical monocytes ($LY6C^+$)—CCR2, nonclassical monocytes ($LY6C^-$)—ENO3 (Casanova-Acebes et al. 2021), alveolar macrophages—LPL, cDC2—CD209A, activated DC—BIRC3, pDCs—BST2, SIGLECH, and regulatory T cells (*Treg*)—FOXP3 and CTLA4.

DE Analysis of Lung Cells Across Species

The same procedures as in DE analysis of gut cells across species were performed for the lung-resident cells. See Go term analysis and enriched pathways for *R. aegyptiacus* AT2 cells in supplementary table S10, Supplementary Material online.

Complement System Gene and Activity Analysis

Detection of Positive Selection in Complement System Genes in Bats

We employed a phylogenetic-based approach to analyze 14 genes involved in the classical and alternative pathways of the complement (C1S, C1R, C2, CFB, CFD, CFI, C3, C5, C6, C7, C9, C8A, C8B, and C8G). We used orthologous genes from up to 10 bat species, representing different branches across Chiroptera (*R. aegyptiacus*, *Pteropus vampirus*, *Rhinolophus ferrumequinum*, *Molossus molossus*, *Phylostomus discolor*, *Artibeus jamaicensis*, *Pteropus_vampirus*, *Pipistrellus kuhlii*, *Myotis myotis*, *Myotis lucifugus*). Orthologous sequences were aligned using MAFFT (Katoh and Standley 2013) with default parameters, and poorly aligned regions were removed (by columns) using GUIDANCE v2.0.2 (Sela et al. 2015) (default parameters). We employed PhyML v3.1 (Guindon et al. 2010) for phylogenetic tree reconstruction for each of the MSAs. Finally, we used codeML from the PAML package v4.9h (Yang 2007) using a site model (NSsites = 8, model = 0). In order to evaluate the null hypothesis against the alternative model, we employed the likelihood-ratio test and calculated the corresponding *P*-value using a χ^2 distribution with 1 degree of freedom, followed by False Discovery Rate (FDR) correction. Positively selected genes were considered those with a corrected *P*-value < 0.05 (8 out 14).To identify sites under positive selection, we utilized the Bayes Empirical Bayes approach. Genes with residues having over 95% probability for positive selection (Pr > 0.95) were considered to exhibit strong evidence of positive selection.

Serum Proteomics Analysis

Blood was collected from four healthy adult male bat individuals and four healthy 10-week-old male C57BL/6 black mice. Freshly collected whole blood was left to clot at room temperature for 30 min. The clot was removed by centrifuging at $1{,}000 \times g$ for 10 min in a refrigerated centrifuge. 100 µL of the serum was lyophilized before shipping for proteomics analysis.

A hundred microlitres of each serum sample was lyophilized and reconstituted in 100 µL of 50 mM ammonium bicarbonate (ABC). Two microlitres of each serum was diluted into 20 µL of 50 mM ABC and disulfide bonds were reduced and alkylated with 10 mM Tris(2-carboxyethyl)phosphine hydrochloride and 40 mM chloroacetamide for 30 min at 37 °C. Proteins were further denatured by adding 2, 2, 2-trifluoroethanol to 20% (v/v) and heated at 95 °C for 5 min. TFE was diluted and 0.4 µg of trypsin (NEB) was added for overnight 37 °C incubation; additional 0.2 µg of trypsin was added for another 3 h incubation at 37 °C. Resulting peptides were cleaned up by C-18 STop And Go Extraction (STAGE) tips (Ishihama et al. 2002) and peptide concentration was estimated using NanoDrop One, 205 nm Scopes (Thermo Scientific). Approximately 80 ng of peptides were injected into timsTOF Pro2 (Bruker Daltonics) coupled to NanoElute UHPLC (Bruker Daltonics) using Aurora Series Gen2 analytical column (IonOpticks) using a DIA-PASEF method. Instrument parameters follows paper PMC10806398 with following method changes. The PASEF ramps contained 25 nonoverlapping

isolation windows from 299.5 to 1200.5 m/z with ion mobility range of 0.7 to 1.3 V s cm^{-2} and collision energy ramped from 20.0 eV at 0.6 V s cm^{-2} to 65.0 eV at 1.6 V s cm^{-2}.

Data was searched against either the Uniprot assembly of *R. aegyptiacus* (UP000593571) or mouse (UP000000589) proteomes with a custom list of contaminants with DIA-NN version 1.8.2 beta 27 (Demichev et al. 2020). Library-free search mode was enabled, using trypsin/P protease specificity and one missed cleavages. Other search parameters include one maximum number of variable modification, N-terminal M excision, carbamidomethylation of C, and oxidation of M. Peptide length ranged 7 to 30, precursor charge ranged 1 to 4, precursor m/z ranged 300 to 1,800, and fragment ion m/z ranged 200 to 1,800. Precursor FDR was set to 1%, with 0 for settings "mass accuracy", "MS1 accuracy", and "scan window". Settings "heuristic protein inference", "use isotopologues", "match between run", and "no shared spectra" were all enabled. "Protein name from FASTA" was chosen for protein inference parameter along with "double-pass mode" for neural network classifier. QuantUMS (high precision) was used for quantification strategy, RT-dependent mode for cross-run normalization, and smart profiling mode for library generation.

We normalized the protein abundance values by dividing the abundance values by the summation of all abundance protein values (and multiplied by 10E6).

Hemolytic Assay Using Rabbit Blood

The hemolytic activity assay was performed as described previously for bacteria and adapted for serum (Glomski et al. 2002). Bat serum was serially diluted in PBS, and incubated with 0.5% rabbit red blood cell suspension, obtained from TAU animal facility from an unrelated experiment. Hemolysis was measured by following the change in absorbance at 540 nm.

PBMC Analysis

Single-cell RNA-seq Quality Control, Clustering and Cell Type Identification

For QC and clustering of *R. aegyptiacus* PBMC single-cell data, we employed a similar approach to the one described above for gut cells, with the exception of using a threshold of cells with <20% mitochondrial reads. *R. aegyptiacus* data were integrated and Leiden-clustered as described in the gut section. Clusters and subclustres were identified using computationally derived marker genes between clusters as well as using known markers from previous studies (Aandahl et al. 2003; Martin and Badovinac 2018; Zhang et al. 2019; Bieberich et al. 2021; Elmentaite et al. 2021; Madissoon et al. 2023).

Rousettus aegyptiacus Cells. Myeloid cells were subdivided into monocytes (MAFB), cDCs (IL18 and CD1A) (Coventry and Heinzel 2004), activated DC (LAMP3, FSCN1, BATF3, and CCR7) and pDCs on the basis of IRF8 and TCF4. Monocytes were further divided into CD14 monocytes (CD14, F13A1, and VCAN) (Casanova-Acebes et al. 2021), CD16 monocytes (FCGR3A and CX3CR1) and a population defined by the expression of IFNB1. Neutrophils were identified as well, based on CSF3R, CCRL2, and G0S2.

The lymphocytes were subdivided into T/NK cells and B cells. The T/NK population was subdivided into T (CD3) CD4 or CD8 expressing cells and NK cells. The CD4-expressing T cells were further divided into naïve T cells on the basis of CCR7, TCF7 and LEF1, CM CD4 T cells, a population with a weaker expression of these genes and EM CD4 T cells, on the basis of CXCR6. Another CD4-expressing population is the regulatory T cells (Tregs), identified by the markers FOXP3 and CTLA4. The CD8-expressing T cells were divided into CM and EM CD8 T cells on the basis of additional expression of GZMB and a lack of the differentiation marker CD7 (Aandahl et al. 2003). NKT and NK cells were identified based on the expression of the KIR receptor KLRD1 together with NCR1, while NK cells lacked the expression of CD3D and CD3G. In a similar manner to CD8 T cells, NKT and NK cells were identified as activated when lacking the expression of CD7 while expressing GZMB.

B cells were identified by the expression of CD79B together with MS4A1 while plasma cells were expressing MZB1 and JCHAIN as well. Another B cell population was annotated based on the additional expression of the activation marker CD83.

Mouse Cells. Mouse datasets were integrated with Seurat CCA and annotations were done as described for *R. aegyptiacus* with the following differences:

For the neutrophils, we used the S100A8 marker as well, for the LY6C2+ monocytes we used the canonical marker LY6C2, for the LY6C2− monocytes—APOE and FCGT4 (Mildner et al. 2017), for the pDCs—BST2 and for the NKT cells we used NKG7 as well.

Comparative Analysis of Expression of Specific Sets of Immune Genes Across Cell Types

To compare gene expression of specific gene sets of interest, we created scores using Scanpy's tl.score_genes() with default parameters. For each cell, a score is the average expression of selected genes subtracted from the average expression of all genes. The score is then standardized to be between 0 and 1. We used three scores representing different stages and pathways known to be upregulated during the innate immune response against pathogens: (i) Inflammatory score: A set of inflammatory response-related and inflammatory cytokine and chemokine genes (Liberzon et al. 2015); (ii) Primary antiviral response score: Primary antiviral response genes were taken from a set of genes upregulated following 4 h of dsRNA-stimulation in dermal fibroblasts taken from previous studies (Hagai et al. 2018; Schneor et al. 2023). The set we used here includes 175 genes that were upregulated in all studied species—*R. aegyptiacus*, mouse and human; and (iii) Interferon response score: 79 ISGs, representing the second wave of response, were taken from a list of ISGs known to be conserved across mammals (Shaw et al. 2017).

DE Analysis of LPS and dsRNA-Stimulation in Monocytes

DE analysis of monocyte stimulation was performed using FindMarkers() of Seurat v3 with default parameters (min.pct = 10, logfc.threshold = 0.25, assay = "RNA"). We compared LPS-stimulated cells to unstimulated cells, and dsRNA-transfected cells to unstimulated cells.

For gene enrichment analysis we used DE genes of stimulated (LPS and dsRNA) and unstimulated bat monocytes. The top 100 genes with the lowest adjusted *P*-values for

each condition were tested for functional enrichment using g:Profiler (Raudvere et al. 2019). We then filtered for terms unique to each condition and plotted these using Python's seaborn barplot.

For producing the numbers of DE genes between different cell types in different conditions, as appears in supplementary table S7, Supplementary Material online, we performed downsampling of the data prior to DE calculations. All cell types in an Unstimulated–Stimulated DE calculation were down-sampled to having the same number of cells as the cell type with the smallest number of cells. Similar procedures of downsasmpling were performed in all DE analysis between species, and/or across cell types and/or conditions.

Analysis of dsRNA-response in *Rousettus aegyptiacus* and *Mouse* Monocytes

Characterization of three States in Monocytes During dsRNA-Stimulation

We divided CD16 monocytes cells into three groups as follows: monocytes were found in two distinct clusters in the UMAP: a cluster with almost exclusively dsRNA-stimulated cells, enriched with IFNB1 expressing cells (termed "IFN monocytes"), and a separate cluster composed of unstimulated, mock-stimulated, and dsRNA-stimulated cells. In the latter cluster, we divided the cells based on those that are dsRNA-stimulated and all others, resulting in a total of three cell sets. In this analysis, we excluded cells from one particular individual that were outliers in the UMAP. We then used DE analysis (using the same functions and parameters as above) to obtain the top upregulated genes in each cell group, by comparing each group of cells to the other two and taking the 100 most significantly upregulated (logFC > 0 and Q-value < 0.01).The expression of the expression of the resulting 300 genes across all CD16 monocyte cells were then clustered and plotted using Python's seaborn.clustermap(). Both genes and cells were clustered using the "ward" clustering method. We then performed GO term analysis on each of the gene groups using g:Profiler (Raudvere et al. 2019).

Conservation of the IFN Monocytes DE Genes Between bat and Mouse

We next defined the groups of *R. aegyptiacus* genes that are uniquely up- and down-regulated in IFN monocytes in comparison with the other two groups (dsRNA monocytes and unstimulated monocytes). This was based on the DE analysis between the three groups described in the previous section. We define 59 genes to be upregulated only in IFN monocytes as those (i) having logFC > 0 and Q-value <0.05 in the IFN monocytes in comparison with the two other groups as well as (ii) not upregulated in other dsRNA-stimulated monocytes. Similarly, we define 725 genes to be uniquely downregulated in IFN monocytes with respect to the other groups of monocytes.

Analysis of Recent IFN Gene Duplicates

Type-I IFN genes in *R. aegyptiacus* genome were detected through their orthology assignments in EggNOG. Log-normalized expression levels of type-I IFN genes that were expressed in *R. aegyptiacus* and mouse cells (IFNB1 and various IFNA and IFNW genes) were plotted in different cell groups in mouse and *R. aegyptiacus* cells using Scanpy's dotplot(). As the expression was almost entirely in the group of IFN monocytes, violin plots of Log-normalized expression of IFN genes were generated using Python's seaborn.violinplot() function using data from this group of cells.

Supplementary Material

Supplementary material is available at *Molecular Biology and Evolution* online.

Acknowledgments

We would like to thank Amit Zeisel, Osnat Hadad Ophir, Muhammad Tibi, Xi Chen, Matthias Friedrich, Roser Vento-Tormo, Luz Garcia-Alonso, Naama Peshes-Yaloz and Stefanos Tsiftsoglou for helpful discussions during the project and on the manuscript. We would like to thank Stefan Kaltenbach and Rami Khosravi for technical assistance with NGS library preparations.

Funding

This research was supported by the Israel Science Foundation (ISF, grant no. 435/20), the Chan Zuckerberg Initiative (Single-Cell Analysis of Inflammation, grant no. DAF2020-217532), by a joint QBI/UCSF-TAU research grant in computational biology and drug discovery (for T.H.). G.D. was supported by the Chan Zuckerberg Initiative (Single-Cell Analysis of Inflammation, Id. DAF2020-217532) and by Fondazione AIRC (Associazione Italiana per la ricerca sul cancro) ETS (IG 2023-Id. 28831). Mass spectrometry infrastructure was supported by the Canada Foundation for Innovation, the BC Knowledge Development Fund, Genome BC (374PRO), and the Life Sciences Institute (for L.J.F.). M.W. was supported by the European Research Council (ERC CoG–Behavior-Island-101001993, for Y.L.). A.A.K. was co-financed by the Polish National Agency for Academic Exchange within the Polish Returns Programme and the National Science Centre, Poland, grant no. 2023/02/1/NZ5/00003.

Data Availability

Raw sequencing data of single-cell and spatial transcriptomics and their processed count matrices with metadata produced in this work are available in ArrayExpress (https://www.ebi.ac.uk/biostudies/arrayexpress/studies) with the following accession numbers: E-MTAB-13276, E-MTAB-13277, E-MTAB-13278, E-MTAB-13280, E-MTAB-13281, E-MTAB-13275, E-MTAB-13279. Previously published human single-cell transcriptomics data are detailed in the relevant sections and can be downloaded from ArrayExpress with the accession numbers E-MTAB-9543, E-MTAB-9536, E-MTAB-9532, E-MTAB-9533, and E-MTAB-10386. The mass spectrometry proteomics data of bat and mouse serum have been deposited to the ProteomeXchange Consortium via the PRIDE (Perez-Riverol et al. 2022) partner repository with the dataset identifier PXD058003. Code generated during this study is available at: https://github.com/HagaiLab/bat_immunty_evolution.

References

Aandahl EM, Sandberg JK, Beckerman KP, Taskén K, Moretto WJ, Nixon DF. CD7 is a differentiation marker that identifies multiple CD8 T cell effector subsets. *J Immunol*. 2003:170(5):2349–2355. https://doi.org/10.4049/jimmunol.170.5.2349.

Ahn M, Anderson DE, Zhang Q, Tan CW, Lim BL, Luko K, Wen M, Chia WN, Mani S, Wang LC, *et al.* Dampened NLRP3-mediated inflammation in bats and implications for a special viral reservoir host. *Nat Microbiol.* 2019:4(5):789–799. https://doi.org/10.1038/s41564-019-0371-3.

Ahn M, Chen VC-W, Rozario P, Ng WL, Kong PS, Sia WR, Kang AEZ, Su Q, Nguyen LH, Zhu F, *et al.* Bat ASC2 suppresses inflammasomes and ameliorates inflammatory diseases. *Cell.* 2023:186(10):2144–2159.e22. https://doi.org/10.1016/j.cell.2023.03.036.

Ahn M, Cui J, Irving AT, Wang L-F. Unique loss of the PYHIN gene family in bats amongst mammals: implications for inflammasome sensing. *Sci Rep.* 2016:6(1):21722. https://doi.org/10.1038/srep21722.

Allaire JM, Crowley SM, Law HT, Chang S-Y, Ko H-J, Vallance BA. The intestinal epithelium: central coordinator of mucosal immunity. *Trends Immunol.* 2018:39(9):677–696. https://doi.org/10.1016/j.it.2018.04.002.

Allan DSJ, Kirkham CL, Aguilar OA, Qu LC, Chen P, Fine JH, Serra P, Awong G, Gommerman JL, Zúñiga-Pflücker JC, *et al.* An in vitro model of innate lymphoid cell function and differentiation. *Mucosal Immunol.* 2015:8(2):340–351. https://doi.org/10.1038/mi.2014.71.

Amman BR, Swanepoel R, Nichol ST, Towner JS. Ecology of filoviruses. *Curr Top Microbiol Immunol.* 2017:411:23–61. https://doi.org/10.1007/82_2017_10.

Avital G, Kuperwaser F, Pountain AW, Lacey KA, Zwack EE, Podkowik M, Shopsin B, Torres VJ, Yanai I. The tempo and mode of gene regulatory programs during bacterial infection. *Cell Rep.* 2022:41(2):111477. https://doi.org/10.1016/j.celrep.2022.111477.

Banerjee A, Baker ML, Kulcsar K, Misra V, Plowright R, Mossman K. Novel insights into immune systems of bats. *Front Immunol.* 2020:11:26. https://doi.org/10.3389/fimmu.2020.00026.

Banerjee A, Kulcsar K, Misra V, Frieman M, Mossman K. Bats and coronaviruses. *Viruses.* 2019:11(1):41. https://doi.org/10.3390/v11010041.

Bergen V, Lange M, Peidli S, Wolf FA, Theis FJ. Generalizing RNA velocity to transient cell states through dynamical modeling. *Nat Biotechnol.* 2020:38(12):1408–1414. https://doi.org/10.1038/s41587-020-0591-3.

Bieberich F, Vazquez-Lombardi R, Yermanos A, Ehling RA, Mason DM, Wagner B, Kapetanovic E, Di Roberto RB, Weber CR, Savic M, *et al.* A single-cell atlas of lymphocyte adaptive immune repertoires and transcriptomes reveals age-related differences in convalescent COVID-19 patients. *Front Immunol.* 2021:12:701085. https://doi.org/10.3389/fimmu.2021.701085.

Breuer K, Foroushani AK, Laird MR, Chen C, Sribnaia A, Lo R, Winsor GL, Hancock REW, Brinkman FSL, Lynn DJ. InnateDB: systems biology of innate immunity and beyond–recent updates and continuing curation. *Nucleic Acids Res.* 2013:41(D1):D1228–D1233. https://doi.org/10.1093/nar/gks1147.

Cagliani R, Forni D, Mozzi A, Fuchs R, Hagai T, Sironi M. Evolutionary analysis of ZAP and its cofactors identifies intrinsically disordered regions as central elements in host-pathogen interactions. *Comput Struct Biotechnol J.* 2024:23:3143–3154. https://doi.org/10.1016/j.csbj.2024.07.022.

Capra JA, Williams AG, Pollard KS. ProteinHistorian: tools for the comparative analysis of eukaryote protein origin. *PLoS Comput Biol.* 2012:8(6):e1002567. https://doi.org/10.1371/journal.pcbi.1002567.

Cardoso-Moreira M, Halbert J, Valloton D, Velten B, Chen C, Shao Y, Liechti A, Ascenção K, Rummel C, Ovchinnikova S, *et al.* Gene expression across mammalian organ development. *Nature.* 2019:571(7766):505–509. https://doi.org/10.1038/s41586-019-1338-5.

Casanova-Acebes M, Dalla E, Leader AM, LeBerichel J, Nikolic J, Morales BM, Brown M, Chang C, Troncoso L, Chen ST, *et al.* Tissue-resident macrophages provide a pro-tumorigenic niche to early NSCLC cells. *Nature.* 2021:595(7868):578–584. https://doi.org/10.1038/s41586-021-03651-8.

Chaudhary N, Jayaraman A, Reinhardt C, Campbell JD, Bosmann M. A single-cell lung atlas of complement genes identifies the mesothelium and epithelium as prominent sources of extrahepatic complement proteins. *Mucosal Immunol.* 2022:15(5):927–939. https://doi.org/10.1038/s41385-022-00534-7.

Clemmensen SN, Bohr CT, Rørvig S, Glenthøj A, Mora-Jensen H, Cramer EP, Jacobsen LC, Larsen MT, Cowland JB, Tanassi JT, *et al.* Olfactomedin 4 defines a subset of human neutrophils. *J Leukoc Biol.* 2012:91(3):495–500. https://doi.org/10.1189/jlb.0811417.

Cohn O, Yankovitz G, Peshes-Yaloz N, Steuerman Y, Frishberg A, Brandes R, Mandelboim M, Hamilton JR, Hagai T, Amit I, *et al.* Distinct gene programs underpinning disease tolerance and resistance in influenza virus infection. *Cell Syst.* 2022:13(12):1002–1015.e9. https://doi.org/10.1016/j.cels.2022.11.004.

Costantini D, Weinberg M, Jordán L, Moreno KR, Yovel Y, Czirják GÁ. Induced bacterial sickness causes inflammation but not blood oxidative stress in Egyptian fruit bats (*Rousettus aegyptiacus*). *Conserv Physiol.* 2022:10(1):coac028. https://doi.org/10.1093/conphys/coac028.

Coventry B, Heinzel S. CD1a in human cancers: a new role for an old molecule. *Trends Immunol.* 2004:25(5):242–248. https://doi.org/10.1016/j.it.2004.03.002.

David D, Davidson I, Karniely S, Edery N, Rosenzweig A, Sol A. Israeli *Rousettus aegyptiacus* Pox virus (IsrRAPXV) infection in Juvenile Egyptian fruit bat (*Rousettus aegyptiacus*): clinical findings and molecular detection. *Viruses.* 2021:13(3):407. https://doi.org/10.3390/v13030407.

Demian WL, Cormier O, Mossman K. Immunological features of bats: resistance and tolerance to emerging viruses. *Trends Immunol.* 2024:45(3):198–210. https://doi.org/10.1016/j.it.2024.01.008.

Demichev V, Messner CB, Vernardis SI, Lilley KS, Ralser M. DIA-NN: neural networks and interference correction enable deep proteome coverage in high throughput. *Nat Methods.* 2020:17(1):41–44. https://doi.org/10.1038/s41592-019-0638-x.

Elmentaite R, Kumasaka N, Roberts K, Fleming A, Dann E, King HW, Kleshchevnikov V, Dabrowska M, Pritchard S, Bolt L, *et al.* Cells of the human intestinal tract mapped across space and time. *Nature.* 2021:597(7875):250–255. https://doi.org/10.1038/s41586-021-03852-1.

Field HE, Mackenzie JS, Daszak P. Henipaviruses: emerging paramyxoviruses associated with fruit bats. *Curr Top Microbiol Immunol.* 2007:315:133–159. https://doi.org/10.1007/978-3-540-70962-6_7.

Fraimovitch E, Hagai T. Promoter evolution of mammalian gene duplicates. *BMC Biol.* 2023:21(1):80. https://doi.org/10.1186/s12915-023-01590-6.

Ge X-Y, Li J-L, Yang X-L, Chmura AA, Zhu G, Epstein JH, Mazet JK, Hu B, Zhang W, Peng C, *et al.* Isolation and characterization of a bat SARS-like coronavirus that uses the ACE2 receptor. *Nature.* 2013:503(7477):535–538. https://doi.org/10.1038/nature12711.

Glomski IJ, Gedde MM, Tsang AW, Swanson JA, Portnoy DA. The Listeria monocytogenes hemolysin has an acidic pH optimum to compartmentalize activity and prevent damage to infected host cells. *J Cell Biol.* 2002:156(6):1029–1038. https://doi.org/10.1083/jcb.200201081.

Guindon S, Dufayard J-F, Lefort V, Anisimova M, Hordijk W, Gascuel O. New algorithms and methods to estimate maximum-likelihood phylogenies: assessing the performance of PhyML 3.0. *Syst Biol.* 2010:59(3):307–321. https://doi.org/10.1093/sysbio/syq010.

Guito JC, Prescott JB, Arnold CE, Amman BR, Schuh AJ, Spengler JR, Sealy TK, Harmon JR, Coleman-McCray JD, Kulcsar KA, *et al.* Asymptomatic infection of Marburg virus reservoir bats is explained by a strategy of immunoprotective disease tolerance. *Curr Biol.* 2021:31(2):257–270.e5. https://doi.org/10.1016/j.cub.2020.10.015.

Hagai T, Chen X, Miragaia RJ, Rostom R, Gomes T, Kunowska N, Henriksson J, Park J-E, Proserpio V, Donati G, *et al.* Gene expression variability across cells and species shapes innate immunity. *Nature.* 2018:563(7730):197–202. https://doi.org/10.1038/s41586-018-0657-2.

Hao Y, Hao S, Andersen-Nissen E, Mauck WM, Zheng S, Butler A, Lee MJ, Wilk AJ, Darby C, Zager M, *et al.* Integrated analysis of multimodal single-cell data. *Cell.* 2021:184(13):3573–3587.e29. https://doi.org/10.1016/j.cell.2021.04.048.

Hayward JA, Tachedjian M, Johnson A, Irving AT, Gordon TB, Cui J, Nicolas A, Smith I, Boyd V, Marsh GA, *et al.* Unique evolution of

antiviral tetherin in bats. *J Virol*. 2022:96(20):e0115222. https://doi.org/10.1128/jvi.01152-22.
Morales AE, Dong Y, Brown T, Baid K, Kontopoulos D-G, Gonzalez V, Huang Z, Ahmed AW, Bhuinya A, Hilgers L, *et al*. Bat genomes illuminate adaptations to viral tolerance and disease resistance. *Nature*. https://doi.org/10.1038/s41586-024-08471-0, 29 January 2025.
Huerta-Cepas J, Szklarczyk D, Heller D, Hernández-Plaza A, Forslund SK, Cook H, Mende DR, Letunic I, Rattei T, Jensen LJ, *et al*. eggNOG 5.0: a hierarchical, functionally and phylogenetically annotated orthology resource based on 5090 organisms and 2502 viruses. *Nucleic Acids Res*. 2019:47(D1):D309–D314. https://doi.org/10.1093/nar/gky1085.
Irving AT, Ahn M, Goh G, Anderson DE, Wang L-F. Lessons from the host defences of bats, a unique viral reservoir. *Nature*. 2021:589(7842):363–370. https://doi.org/10.1038/s41586-020-03128-0.
Irving AT, Zhang Q, Kong P-S, Luko K, Rozario P, Wen M, Zhu F, Zhou P, Ng JHJ, Sobota RM, *et al*. Interferon regulatory factors IRF1 and IRF7 directly regulate gene expression in bats in response to viral infection. *Cell Rep*. 2020:33(5):108345. https://doi.org/10.1016/j.celrep.2020.108345.
Ishihama Y, Rappsilber J, Andersen JS, Mann M. Microcolumns with self-assembled particle frits for proteomics. *J Chromatogr A*. 2002:979(1-2):233–239. https://doi.org/10.1016/S0021-9673(02)01402-4.
Jacquet S, Culbertson M, Zhang C, El Filali A, De La Myre Mory C, Pons J-B, Filippi-Codaccioni O, Lauterbur ME, Ngoubangoye B, Duhayer J, *et al*. Adaptive duplication and genetic diversification of protein kinase R contribute to the specificity of bat-virus interactions. *Sci Adv*. 2022:8(47):eadd7540. https://doi.org/10.1126/sciadv.add7540.
James KR. Transcriptional diversity along the intestinal crypt-villi axis. *Nat Rev Genet*. 2024:25(4):235–235. https://doi.org/10.1038/s41576-024-00700-6.
Jayaprakash AD, Ronk AJ, Prasad AN, Covington MF, Stein KR, Schwarz TM, Hekmaty S, Fenton KA, Geisbert TW, Basler CF, *et al*. Marburg and ebola virus infections elicit a complex, muted inflammatory state in bats. *Viruses*. 2023:15(2):350. https://doi.org/10.3390/v15020350.
Jebb D, Huang Z, Pippel M, Hughes GM, Lavrichenko K, Devanna P, Winkler S, Jermiin LS, Skirmuntt EC, Katzourakis A, *et al*. Six reference-quality genomes reveal evolution of bat adaptations. *Nature*. 2020:583(7817):578–584. https://doi.org/10.1038/s41586-020-2486-3.
Katoh K, Standley DM. MAFFT multiple sequence alignment software version 7: improvements in performance and usability. *Mol Biol Evol*. 2013:30(4):772–780. https://doi.org/10.1093/molbev/mst010.
Kleshchevnikov V, Shmatko A, Dann E, Aivazidis A, King HW, Li T, Elmentaite R, Lomakin A, Kedlian V, Gayoso A, *et al*. Cell2location maps fine-grained cell types in spatial transcriptomics. *Nat Biotechnol*. 2022:40(5):661–671. https://doi.org/10.1038/s41587-021-01139-4.
Kumasaka N, Rostom R, Huang N, Polanski K, Meyer KB, Patel S, Boyd R, Gomez C, Barnett SN, Panousis NI, *et al*. Mapping interindividual dynamics of innate immune response at single-cell resolution. *Nat Genet*. 2023:55(6):1066–1075. https://doi.org/10.1038/s41588-023-01421-y.
Kuzmin IV, Schwarz TM, Ilinykh PA, Jordan I, Ksiazek TG, Sachidanandam R, Basler CF, Bukreyev A. Innate immune responses of bat and human cells to filoviruses: commonalities and distinctions. *J Virol*. 2017:91(8):e02471-16. https://doi.org/10.1128/JVI.02471-16.
Larson PA, Bartlett ML, Garcia K, Chitty J, Balkema-Buschmann A, Towner J, Kugelman J, Palacios G, Sanchez-Lockhart M. Genomic features of humoral immunity support tolerance model in Egyptian rousette bats. *Cell Rep*. 2021:35(7):109140. https://doi.org/10.1016/j.celrep.2021.109140.
Lehrer RI, Lu W. α-Defensins in human innate immunity. *Immunol Rev*. 2012:245(1):84–112. https://doi.org/10.1111/j.1600-065X.2011.01082.x.
Levin D, Schneider WM, Hoffmann H-H, Yarden G, Busetto AG, Manor O, Sharma N, Rice CM, Schreiber G. Multifaceted activities of type I interferon are revealed by a receptor antagonist. *Sci Signal*. 2014:7(327):ra50. https://doi.org/10.1126/scisignal.2004998.
Li W, Shi Z, Yu M, Ren W, Smith C, Epstein JH, Wang H, Crameri G, Hu Z, Zhang H, *et al*. Bats are natural reservoirs of SARS-like coronaviruses. *Science*. 2005:310(5748):676–679. https://doi.org/10.1126/science.1118391.
Liberzon A, Birger C, Thorvaldsdóttir H, Ghandi M, Mesirov JP, Tamayo P. The molecular signatures database (MSigDB) hallmark gene set collection. *Cell Syst*. 2015:1(6):417–425. https://doi.org/10.1016/j.cels.2015.12.004.
Madissoon E, Oliver AJ, Kleshchevnikov V, Wilbrey-Clark A, Polanski K, Richoz N, Ribeiro Orsi A, Mamanova L, Bolt L, Elmentaite R, *et al*. A spatially resolved atlas of the human lung characterizes a gland-associated immune niche. *Nat Genet*. 2023:55(1):66–77. https://doi.org/10.1038/s41588-022-01243-4.
Martin MD, Badovinac VP. Defining memory CD8 T cell. *Front Immunol*. 2018:9:2692. https://doi.org/10.3389/fimmu.2018.02692.
Mildner A, Schönheit J, Giladi A, David E, Lara-Astiaso D, Lorenzo-Vivas E, Paul F, Chappell-Maor L, Priller J, Leutz A, *et al*. Genomic characterization of murine monocytes reveals C/EBPβ transcription factor dependence of Ly6C-cells. *Immunity*. 2017:46(5):849–862.e7. https://doi.org/10.1016/j.immuni.2017.04.018.
Moor AE, Harnik Y, Ben-Moshe S, Massasa EE, Rozenberg M, Eilam R, Bahar Halpern K, Itzkovitz S. Spatial reconstruction of single enterocytes uncovers broad zonation along the intestinal villus axis. *Cell*. 2018:175(4):1156–1167.e15. https://doi.org/10.1016/j.cell.2018.08.063.
Moreno KR, Weinberg M, Harten L, Salinas Ramos VB, Herrera M LG, Czirják GÁ, Yovel Y. Sick bats stay home alone: fruit bats practice social distancing when faced with an immunological challenge. *Ann N Y Acad Sci*. 2021:1505(1):178–190. https://doi.org/10.1111/nyas.14600.
Moreno Santillán DD, Lama TM, Gutierrez Guerrero YT, Brown AM, Donat P, Zhao H, Rossiter SJ, Yohe LR, Potter JH, Teeling EC, *et al*. Large-scale genome sampling reveals unique immunity and metabolic adaptations in bats. *Mol Ecol*. 2021:30(23):6449–6467. https://doi.org/10.1111/mec.16027.
Murat F, Mbengue N, Winge SB, Trefzer T, Leushkin E, Sepp M, Cardoso-Moreira M, Schmidt J, Schneider C, Mößinger K, *et al*. The molecular evolution of spermatogenesis across mammals. *Nature*. 2023:613(7943):308–316. https://doi.org/10.1038/s41586-022-05547-7.
Niec RE, Chu T, Schernthanner M, Gur-Cohen S, Hidalgo L, Pasolli HA, Luckett KA, Wang Z, Bhalla SR, Cambuli F, *et al*. Lymphatics act as a signaling hub to regulate intestinal stem cell activity. *Cell Stem Cell*. 2022:29(7):1067–1082.e18. https://doi.org/10.1016/j.stem.2022.05.007.
O'Neill MB, Quach H, Pothlichet J, Aquino Y, Bisiaux A, Zidane N, Deschamps M, Libri V, Hasan M, Zhang S-Y, *et al*. Single-cell and bulk RNA-sequencing reveal differences in monocyte susceptibility to influenza A virus infection between Africans and Europeans. *Front Immunol*. 2021:12:768189. https://doi.org/10.3389/fimmu.2021.768189.
O'Shea TJ, Cryan PM, Hayman DTS, Plowright RK, Streicker DG. Multiple mortality events in bats: a global review. *Mamm Rev*. 2016:46(3):175–190. https://doi.org/10.1111/mam.12064.
Pavlovich SS, Darling T, Hume AJ, Davey RA, Feng F, Mühlberger E, Kepler TB. Egyptian Rousette IFN-ω subtypes elicit distinct antiviral effects and transcriptional responses in conspecific cells. *Front Immunol*. 2020:11:435. https://doi.org/10.3389/fimmu.2020.00435.
Pavlovich SS, Lovett SP, Koroleva G, Guito JC, Arnold CE, Nagle ER, Kulcsar K, Lee A, Thibaud-Nissen F, Hume AJ, *et al*. The Egyptian rousette genome reveals unexpected features of bat antiviral immunity. *Cell*. 2018:173(5):1098–1110.e18. https://doi.org/10.1016/j.cell.2018.03.070.
Paweska JT, Storm N, Grobbelaar AA, Markotter W, Kemp A, Jansen van Vuren P. Experimental inoculation of Egyptian fruit bats

(Rousettus aegyptiacus) with Ebola virus. *Viruses*. 2016:8(2):29. https://doi.org/10.3390/v8020029.
Perez-Riverol Y, Bai J, Bandla C, García-Seisdedos D, Hewapathirana S, Kamatchinathan S, Kundu DJ, Prakash A, Frericks-Zipper A, Eisenacher M, *et al.* The PRIDE database resources in 2022: a hub for mass spectrometry-based proteomics evidences. *Nucleic Acids Res*. 2022:50(D1):D543–D552. https://doi.org/10.1093/nar/gkab1038.
Peterson LW, Artis D. Intestinal epithelial cells: regulators of barrier function and immune homeostasis. *Nat Rev Immunol*. 2014:14(3):141–153. https://doi.org/10.1038/nri3608.
Raudvere U, Kolberg L, Kuzmin I, Arak T, Adler P, Peterson H, Vilo J. G:Profiler: a web server for functional enrichment analysis and conversions of gene lists (2019 update). *Nucleic Acids Res*. 2019:47(W1):W191–W198. https://doi.org/10.1093/nar/gkz369.
Schneor L, Kaltenbach S, Friedman S, Tussia-Cohen D, Nissan Y, Shuler G, Fraimovitch E, Kolodziejczyk AA, Weinberg M, Donati G, *et al.* Comparison of antiviral responses in two bat species reveals conserved and divergent innate immune pathways. *iScience*. 2023:26(8):107435. https://doi.org/10.1016/j.isci.2023.107435.
Schountz T, Baker ML, Butler J, Munster V. Immunological control of viral infections in bats and the emergence of viruses highly pathogenic to humans. *Front Immunol*. 2017:8:1098. https://doi.org/10.3389/fimmu.2017.01098.
Schupp JC, Adams TS, Cosme C, Raredon MSB, Yuan Y, Omote N, Poli S, Chioccioli M, Rose K-A, Manning EP, *et al.* Integrated single-cell atlas of endothelial cells of the human lung. *Circulation*. 2021:144(4):286–302. https://doi.org/10.1161/CIRCULATIONAHA.120.052318.
Sela I, Ashkenazy H, Katoh K, Pupko T. GUIDANCE2: accurate detection of unreliable alignment regions accounting for the uncertainty of multiple parameters. *Nucleic Acids Res*. 2015:43(W1):W7–W14. https://doi.org/10.1093/nar/gkv318.
Selim A, El Nahas E. Comparative histological studies on the intestinal wall between the prenatal, the postnatal and the adult of the two species of Egyptian bats. Frugivorous *Rousettus aegyptiacus* and insectivorous *Taphozous nudiventris*. *J Basic Appl Zool*. 2015:70:25–32. https://doi.org/10.1016/j.jobaz.2015.04.004.
Shaw AE, Hughes J, Gu Q, Behdenna A, Singer JB, Dennis T, Orton RJ, Varela M, Gifford RJ, Wilson SJ, *et al.* Fundamental properties of the mammalian innate immune system revealed by multispecies comparison of type I interferon responses. *PLoS Biol*. 2017:15(12):e2004086. https://doi.org/10.1371/journal.pbio.2004086.
Stephenson E, Reynolds G, Botting RA, Calero-Nieto FJ, Morgan MD, Tuong ZK, Bach K, Sungnak W, Worlock KB, Yoshida M, *et al.* Single-cell multi-omics analysis of the immune response in COVID-19. *Nat Med*. 2021:27(5):904–916. https://doi.org/10.1038/s41591-021-01329-2.
Strine MS, Wilen CB. Tuft cells are key mediators of interkingdom interactions at mucosal barrier surfaces. *PLoS Pathog*. 2022:18(3):e1010318. https://doi.org/10.1371/journal.ppat.1010318.
Tedman RA, Hall LS. The morphology of the gastrointestinal tract and food transit time in the fruit bats *Pteropus alecto* and P. poliocephalus (Megachiroptera). *Aust J Zool*. 1985:33(5):625. https://doi.org/10.1071/ZO9850625.
Temmam S, Vongphayloth K, Baquero E, Munier S, Bonomi M, Regnault B, Douangboubpha B, Karami Y, Chrétien D, Sanamxay D, *et al.* Bat coronaviruses related to SARS-CoV-2 and infectious for human cells. *Nature*. 2022:604(7905):330–336. https://doi.org/10.1038/s41586-022-04532-4.
Tian S, Zeng J, Jiao H, Zhang D, Zhang L, Lei C-Q, Rossiter SJ, Zhao H. Comparative analyses of bat genomes identify distinct evolution of immunity in old world fruit bats. *Sci Adv*. 2023:9(18):eadd0141. https://doi.org/10.1126/sciadv.add0141.
Tirosh I, Izar B, Prakadan SM, Wadsworth MH, Treacy D, Trombetta JJ, Rotem A, Rodman C, Lian C, Murphy G, *et al.* Dissecting the multicellular ecosystem of metastatic melanoma by single-cell RNA-seq. *Science*. 2016:352(6282):189–196. https://doi.org/10.1126/science.aad0501.
Travaglini KJ, Nabhan AN, Penland L, Sinha R, Gillich A, Sit RV, Chang S, Conley SD, Mori Y, Seita J, *et al.* A molecular cell atlas of the human lung from single-cell RNA sequencing. *Nature*. 2020:587(7835):619–625. https://doi.org/10.1038/s41586-020-2922-4.
Tsukui T, Sun K-H, Wetter JB, Wilson-Kanamori JR, Hazelwood LA, Henderson NC, Adams TS, Schupp JC, Poli SD, Rosas IO, *et al.* Collagen-producing lung cell atlas identifies multiple subsets with distinct localization and relevance to fibrosis. *Nat Commun*. 2020:11(1):1920. https://doi.org/10.1038/s41467-020-15647-5.
van der Flier LG, Clevers H. Stem cells, self-renewal, and differentiation in the intestinal epithelium. *Annu Rev Physiol*. 2009:71(1):241–260. https://doi.org/10.1146/annurev.physiol.010908.163145.
Vicente-Santos A, Lock LR, Allira M, Dyer KE, Dunsmore A, Tu W, Volokhov DV, Herrera C, Lei G-S, Relich RF, *et al.* Serum proteomics reveals a tolerant immune phenotype across multiple pathogen taxa in wild vampire bats. *Front Immunol*. 2023:14:1281732. https://doi.org/10.3389/fimmu.2023.1281732.
Vieira Braga FA, Kar G, Berg M, Carpaij OA, Polanski K, Simon LM, Brouwer S, Gomes T, Hesse L, Jiang J, *et al.* A cellular census of human lungs identifies novel cell states in health and in asthma. *Nat Med*. 2019:25(7):1153–1163. https://doi.org/10.1038/s41591-019-0468-5.
Wang L-F, Gamage AM, Chan WOY, Hiller M, Teeling EC. Decoding bat immunity: the need for a coordinated research approach. *Nat Rev Immunol*. 2021:21(5):269–271. https://doi.org/10.1038/s41577-021-00523-0.
Weinberg M, Mazar O, Rachum A, Chen X, Goutink S, Lifshitz N, Winter-Livneh R, Czirják GÁ, Yovel Y. Seasonal challenges of tropical bats in temperate zones. *Sci Rep*. 2022:12(1):16869. https://doi.org/10.1038/s41598-022-21076-9.
Wolf FA, Angerer P, Theis FJ. SCANPY: large-scale single-cell gene expression data analysis. *Genome Biol*. 2018:19(1):15. https://doi.org/10.1186/s13059-017-1382-0.
Wolock SL, Lopez R, Klein AM. Scrublet: computational identification of cell doublets in single-cell transcriptomic data. *Cell Syst*. 2019:8(4):281–291.e9. https://doi.org/10.1016/j.cels.2018.11.005.
Wu J, Zhang L, Shen C, Sin SYW, Lei C, Zhao H. Comparative transcriptome analysis reveals molecular adaptations underlying distinct immunity and inverted resting posture in bats. *Integr Zool*. 2023:18(3):493–505. https://doi.org/10.1111/1749-4877.12676.
Xie CB, Jane-Wit D, Pober JS. Complement membrane attack complex: new roles, mechanisms of action, and therapeutic targets. *Am J Pathol*. 2020:190(6):1138–1150. https://doi.org/10.1016/j.ajpath.2020.02.006.
Yang Z. PAML 4: phylogenetic analysis by maximum likelihood. *Mol Biol Evol*. 2007:24(8):1586–1591. https://doi.org/10.1093/molbev/msm088.
Zelek WM, Harrison RA. Complement and COVID-19: three years on, what we know, what we don't know, and what we ought to know. *Immunobiology*. 2023:228(3):152393. https://doi.org/10.1016/j.imbio.2023.152393.
Zhang Q, He Y, Luo N, Patel SJ, Han Y, Gao R, Modak M, Carotta S, Haslinger C, Kind D, *et al.* Landscape and dynamics of single immune cells in hepatocellular carcinoma. *Cell*. 2019:179(4):829–845.e20. https://doi.org/10.1016/j.cell.2019.10.003.
Zheng GXY, Terry JM, Belgrader P, Ryvkin P, Bent ZW, Wilson R, Ziraldo SB, Wheeler TD, McDermott GP, Zhu J, *et al.* Massively parallel digital transcriptional profiling of single cells. *Nat Commun*. 2017:8(1):14049. https://doi.org/10.1038/ncomms14049.
Zhou P, Cowled C, Mansell A, Monaghan P, Green D, Wu L, Shi Z, Wang L-F, Baker ML. IRF7 in the Australian black flying fox, *Pteropus alecto*: evidence for a unique expression pattern and functional conservation. *PLoS One*. 2014:9(8):e103875. https://doi.org/10.1371/journal.pone.0103875.
Zhou P, Tachedjian M, Wynne JW, Boyd V, Cui J, Smith I, Cowled C, Ng JHJ, Mok L, Michalski WP, *et al.* Contraction of the type I IFN locus and unusual constitutive expression of IFN-α in bats. *Proc Natl Acad Sci U S A*. 2016:113(10):2696–2701. https://doi.org/10.1073/pnas.1518240113.
Zhou P, Yang X-L, Wang X-G, Hu B, Zhang L, Zhang W, Si H-R, Zhu Y, Li B, Huang C-L, *et al.* A pneumonia outbreak associated with a new coronavirus of probable bat origin. *Nature*. 2020:579(7798):270–273. https://doi.org/10.1038/s41586-020-2012-7.